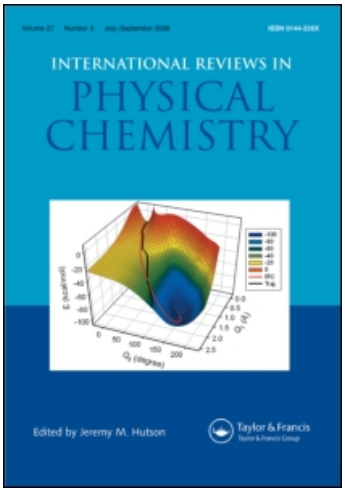

International Reviews in Physical Chemistry
Publication details, including instructions for authors and subscription information:
http://www.informaworld.com/smpp/title~content=t713724383

Excited state hydrogen atom transfer in ammonia-wire and water-wire clusters

Carine Manca[a]; Christian Tanner[a]; Samuel Leutwyler[a]
[a] Departement für Chemie und Biochemie, CH-3012 Bern, Switzerland

To cite this Article Manca, Carine , Tanner, Christian and Leutwyler, Samuel(2005) 'Excited state hydrogen atom transfer in ammonia-wire and water-wire clusters', International Reviews in Physical Chemistry, 24: 3, 457 — 488
To link to this Article: DOI: 10.1080/01442350500390912
URL: http://dx.doi.org/10.1080/01442350500390912

International Reviews in Physical Chemistry,
Vol. 24, Nos. 3–4, July–December 2005, 457–488

Taylor & Francis
Taylor & Francis Group

Excited state hydrogen atom transfer in ammonia-wire and water-wire clusters

CARINE MANCA†, CHRISTIAN TANNER
and SAMUEL LEUTWYLER*

Departement für Chemie und Biochemie, Freiestrasse 3,
CH-3012 Bern, Switzerland

(*Received 21 July 2005; in final form 3 October 2005*)

We review experimental and theoretical investigations of excited-state hydrogen atom transfer (ESHAT) reactions along unidirectionally hydrogen bonded solvent 'wire' clusters. The solvent wire is attached to the aromatic 'scaffold' molecule 7-hydroxyquinoline (7HQ), which offers an O–H and an N hydrogen bonding site, spaced far enough apart to form two- to four-membered wires. $S_1 \leftarrow S_0$ photoexcitation renders the O–H group more acidic and the quinolinic N more basic. This provides a driving force for the enol $\rightarrow$ keto tautomerization, probed by the characteristic fluorescence of the 7-ketoquinoline in the molecular beam experiments. For 7-hydroxyquinoline$\cdot(NH_3)_3$, excitation of ammonia-wire vibrations induces the tautomerization at $\sim$200 cm^{-1}. Different reaction pathways have been explored by excited-state *ab initio* calculations. These show that the reaction proceeds by H-atom transfer along the wire as a series of Grotthus-type translocation steps. There is no competition with a mechanism involving successive proton translocations. The rate-controlling S_1 state barriers arise from crossings of a $\pi\pi^*$ with a Rydberg-type $\pi\sigma^*$ state and the proton and electron movements along the wire are closely coupled. The excited state reactant, H-transferred intermediates and product structures are characterized. The reaction proceeds by tunnelling, as shown by deuteration of the solvent molecules (ND_3) in the wire. The first step of the reaction exhibits intra/intermolecular vibrational mode selectivity. Substitution of NH_3 by one, two or three H_2O molecules in the wire leads to increasing threshold with each additional H_2O molecule, up to $>$2000 cm^{-1} for the 7-hydroxyquinoline$\cdot(H_2O)_3$ water-wire cluster. No 7-ketoquinoline fluorescence is observed upon insertion of even a single H_2O molecule. The calculations show that insertion of each H_2O molecule into the solvent wire introduces a high barrier, which blocks any further H-atom transfer.

Contents

*Corresponding author. Email: leutwyler@iac.unibe.ch
†Current address: Lab. f. Physikalische Chemie, ETH-Hönggerberg, CH-8093 Zürich, Switzerland.

International Reviews in Physical Chemistry
ISSN 0144–235X print/ISSN 1366–591X online
http://www.tandf.co.uk/journals
DOI: 10.1080/01442350500390912

1. Introduction

Proton and hydrogen atom transfer reactions in aqueous solutions are involved in a large variety of chemical and biological processes [1–15]. Hence the measurement, modelling and theory of proton and hydrogen transfers at the atomic level are among the most important challenges in physical chemistry. Proton transport through transmembrane ion channels ('proton wires') is of special interest, since the energetics of cells is intimately connected to the creation, control or utilization of proton gradients across the cell membranes. Hydrogen-bonded wires of water molecules have been identified in membrane-spanning proteins such as bacteriorhodopsin [16–21], the photosynthetic reaction centre [22, 23], the transmembrane channel formed by gramicidin [24–26] and other voltage-gated proton channels [27]. The enzymes carbonic anhydrase [28, 29] and alcohol dehydrogenase [29] also contain proton relays along chains of water molecules embedded in the interior of the protein. The translocation mechanisms along these 'proton wires' have become fields of intense theoretical study [5, 6, 8, 24–26, 28–32].

In other cases, however, the existence of a transmembrane water wire does *not* result in proton translocation: The aquaporins allow efficient single file transfer of water molecules through cell membranes [33–35], whereas the translocation of protons along this water wire is blocked. This proton/water selectivity has been attributed to orientational effects that are believed to destroy the perfect translocation path along the water wire, but it has also been pointed out that a large part of the barrier is the (mostly electrostatic) desolvation penalty of moving the proton charge from bulk solution to water molecules in the channel interior [36–40].

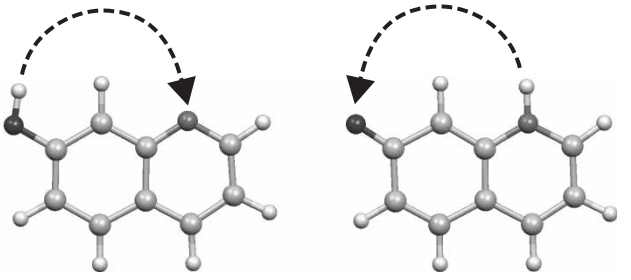

Figure 1. 7-hydroxyquinoline (left) and its tautomeric form 7-ketoquinoline (right). Arrows indicate the hydrogen bond directionality of the solvent wires (donor to acceptor).

Direct molecular-level experimental observation of the motion of protons or H-atoms along hydrogen-bonded solvent wires would help in understanding the factors controlling proton conduction. At ambient temperatures this is difficult to achieve because of the very short times, microscopic length scales, and solvent fluctuations involved. The development of an atomic-level description of these reactions has long been of fundamental interest [2–15, 41]. Experimentally, some of the complexity associated with proton or H-atom transfer along hydrogen bonded solvent wires can be avoided by isolating and supersonically cooling model cluster systems. Such studies allow the investigation of reactions with precisely controlled preparation of reactants and detection of products.

Here we focus on simple model systems in order to understand the basic aspects of proton and/or H-atom conduction along hydrogen-bonded solvent wires. We employ the 7-hydroxyquinoline (7HQ) molecule, shown in figure 1, which exhibits several interesting properties:

(1) It provides a scaffold with two hydrogen bond attachment points, to which a solvent 'wire' may be connected by terminal hydrogen bonds.
(2) The 7HQ scaffold induces a unidirectional (homodromic) hydrogen bond pattern via its hydrogen bond donor and acceptor groups, see figure 1.
(3) 7HQ exhibits large changes in acid/base properties upon electronic excitation. In the S_1 state the O–H group becomes more acidic and the ring nitrogen more basic. This allows one to drive the proton (or H-atom) from the O–H group along the H-bonded solvent wire.
(4) The proton and/or H-atom conduction along the wire results in an excited-state enol $\rightarrow$ keto tautomerization reaction, yielding excited-state 7-ketoquinoline (7KQ*). Simultaneously, the unidirectional H-bond pattern is inverted, cf. figure 1.
(5) The keto form is stabilized in the S_1 state and therefore its fluorescence is strongly red-shifted relative to the enol and can be employed to probe the occurrence of the proton/H-atom transfer reaction.

Below, we discuss and compare results on pure ammonia (NH_3) wires, water (H_2O) wires and mixed NH_3/H_2O wires.

2. 7-Hydroxyquinoline

2.1. *Ground and excited state acid/base properties*

Figure 2 shows 7-hydroxyquinoline (7HQ), the 7-ketoquinoline (7KQ) tautomer as well as the protonated $7H_2Q^+$ and deprotonated $7Q^-$ forms. The zwitterion Z represents a different valence bond resonance structure of 7KQ that emphasizes the large dipole moment of the 7-ketoquinoline tautomer.

Figure 3 summarizes these acid/base properties in a diagram of α (degree of dissociation) vs. pH for the S_0 and S_1 states [42]. In aqueous solution the neutral forms 7HQ and 7KQ exist over a rather narrow range of pH $\approx$ 6–8. Upon electronic excitation, the pK_a of the O–H group decreases from 8.7 (S_0) to -2.7 in the S_1 state [42], while the pK_a of the protonated quinolinic N–H^+ site increases from 5.6 in S_0 to 13.5 in S_1. Not only is the existence range of the neutral form much wider in the S_1 state but the

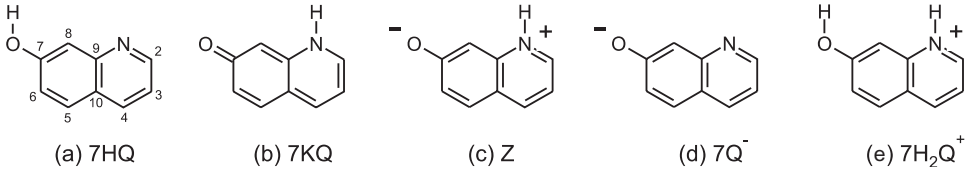

Figure 2. 7-hydroxyquinoline in its enol form (a), the tautomer 7-ketoquinoline (b), the zwitterionic (c), anionic (d), and cationic (e) forms.

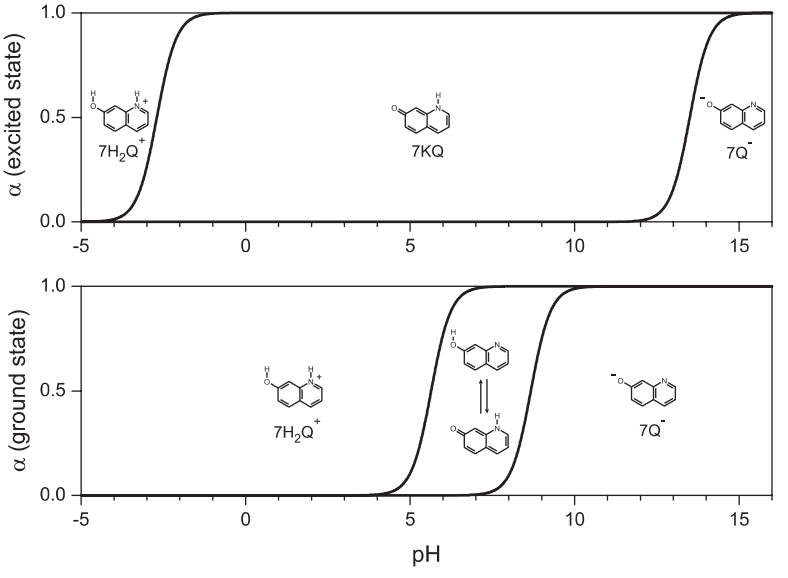

Figure 3. Degree of dissociation α vs. pH in aqueous solution for the different forms of 7HQ in the S_0 and S_1 states.

7HQ $\rightleftharpoons$ 7KQ equilibrium lies strongly on the 7KQ side. Excitation of $7H_2Q^+$ in the pH range of -2 to 5 leads to formation of excited 7KQ. Similarly, the quinolinic N becomes so basic in the S_1 state that even at pH = 12, 7KQ is formed in the excited state. Extreme pHs (<-2.7 for the cation or >13.5 for the anion) are necessary in order to see fluorescence from either the anionic or the cationic form.

The forms of 7HQ in figure 2(a)–(e) have been extensively characterized by absorption and fluorescence spectroscopies in non-polar, polar and protic solvents [42–46]. The peak emission of the 7HQ is in the 370–390 nm range, depending on the solvent. The 7KQ emission is at 525–580 nm, strongly red-shifted relative to the enol. The emission bands of both H_2Q^+ and $7Q^-$ lie in the 430–450 nm range. All four emission bands can be used as diagnostic probes for proton and/or H-atom transfer reactions. The changes in acid/base properties of 7HQ upon electronic excitation have also led to picosecond kinetic studies in various solvents [47–58].

2.2. *O–H bond breaking in the $\pi\pi^*$ and $\pi\sigma^*$ states*

The first step of the 7HQ $\rightarrow$ 7KQ tautomerization reaction must involve either homo- or heterolytic dissociation of the O–H bond. Heterolytic bond cleavage results in proton abstraction, whereas homolytic cleavage leads to hydrogen abstraction. Excited state hydrogen detachment and hydrogen atom transfer reactions of hydroxyaromatic and heteroaromatic molecules have been theoretically investigated by Domcke and Sobolewski [59–65]. They have shown that the $^1\pi\pi^*$ excited states of heteroaromatic molecules are often coupled to repulsive $^1\pi\sigma^*$ excited states along the O–H or N–H bond stretching coordinate. The $^1\pi\sigma^*$ states are dominated by an excitation of an electron from the π HOMO to the diffuse Rydberg-type σ^* orbital shown in figure 4 and are not accessible from the electronic ground state by direct absorption. They usually induce O–H or N–H bond cleavage, as has been shown in studies on phenol, phenol$\cdot H_2O$ and phenol$\cdot NH_3$, indole, pyrrole, adenine and the guanine–cytosine base pair [59–69]. Such intersections of $\pi\sigma^*$ with $\pi\pi^*$ excited states represent a new type of photochemical reaction pathway [64].

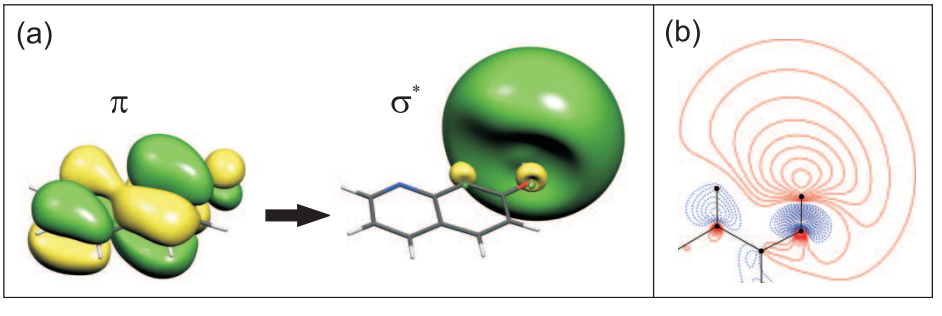

Figure 4. (a) Dominant one-electron excitation of $\pi\sigma^*$ excited state of 7-hydroxyquinoline. The same contour value was used for the π and σ^* orbitals. (b) Cross-section of the σ orbital through the 7HQ molecular plane, showing the antibonding character along the O–H bond.

In order to investigate the importance of $\pi\sigma^*$ excited states for 7HQ photochemistry, we calculated potential energy curves for the S_0 and the lower $\pi\pi^*$ and $\pi\sigma^*$ excited states. The O–H distance was kept frozen at different values between 0.9 and 2.4 Å, all remaining degrees of freedom were allowed to relax for each state individually. All geometry optimizations were performed using Complete Active Space SCF wavefunctions correlating eight electrons in eight orbitals, i.e. (8,8)-CASSCF. The standard 6-31G(d,p) basis set was augmented with diffuse s and p functions ($\alpha_s = \alpha_p = 0.02$) centred on a floating dummy atom. The position of the dummy centre was optimized together with the other degrees of freedom. For the ground state and the $\pi\pi^*$ excited states, the four π and four π^* orbitals that dominate the $\pi\pi^*$ state wavefunction formed the active space whereas for the $\pi\sigma^*$ state the least important π^* orbital was replaced by the σ^* orbital shown in figure 4.

To account for dynamical correlation effects, multireference second-order Møller–Plesset (MRMP2) calculations were performed at the (8,8)-CASSCF optimized geometries. The MRMP2 potential energy curves along the O–H bond dissociation coordinate are shown in figure 5. The $\pi\sigma^*$ potential energy curve crosses both the $\pi\pi^*$ excited state and ground state curves, giving rise to two conical intersections, as for indole and phenol [61, 63]. If one takes non-planar geometries into account, avoided crossings occur. The $\pi\sigma^*$ curve crosses the $\pi\pi^*$ curve at $\sim$11 500 cm^{-1} above the $\pi\pi^*$ minimum, which is significantly higher than in phenol [63] and indole [61].

These crossings which are generally found for heteroaromatics can serve as efficient routes for radiationless relaxation to the electronic ground state. If sufficient vibrational energy is present in the $^1\pi\pi^*$ state, the system can gain access to the repulsive $^1\pi\sigma^*$ state by means of a pathway 'around' the first conical intersection formed by the crossing of the $\pi\pi^*$ and $\pi\sigma^*$ states, cf. figure 5. Upon reaching the second intersection point of the $\pi\sigma^*$ with the S_0 state, the funnel formed by the conical intersection relaxes the system efficiently to the ground state.

As noted above, the O–H bond can be cleaved heterolytically, leading to the $7Q^-$ anion and H^+, or homolytically, leading to the 7-quinolinyl radical $7Q^\bullet$ and a ground-state H(1s) atom. We calculated both $7Q^-$ and $7Q^\bullet$ using the MRMP2 method. The homolytic dissociation is favoured by more than 270 kcal/mol. The sum of the energies of $7Q^\bullet$ and the H(1s) atom is indicated in figure 5 and connects smoothly to the $\pi\sigma^*$ potential energy curve. At the MRMP2 level, the $7Q^- + H^+$ dissociation limit is 98 000 cm^{-1} above the homolytic limit. Therefore, both the S_0 ground and the $\pi\pi^*$ excited state also undergo homolytic dissociation along the O–H coordinate and correlate with excited states of the $7Q^\bullet$ radical (not shown in figure 5). These excited states are essentially described by excitations from the highest doubly occupied MOs to the singly occupied MO (SOMO excited states), the lowest of which are in the near infrared.

The σ^* orbital shown in figure 4 is diffuse or Rydberg-like only at short O–H distances $<$1.2 Å; at larger distances, it contracts considerably. As the dummy centre carries only diffuse functions, whereas the H-atom carries a compact valence 1s plus 2p polarization function set, the size of the σ^* orbital can be quantified in terms of the Mulliken atomic populations of these two centres. In figure 6 one clearly sees that the population of the dummy centre with the diffuse functions decreases rapidly for O–H distances $>$1.2 Å and is no longer important for the description of the σ^* orbital.

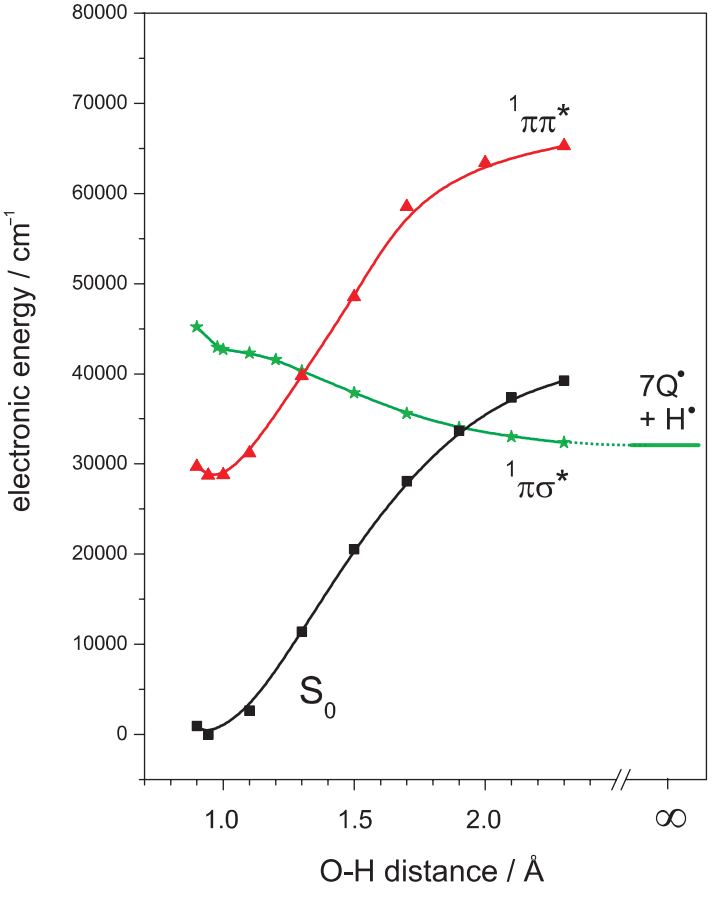

Figure 5. MRMP2 potential energy curves for O–H bond breaking in the electronic ground state and the lowest excited states of A′ ($\pi\pi^*$) and A″ ($\pi\sigma^*$) symmetry of 7-hydroxyquinoline.

3. The 7-hydroxyquinoline·$(NH_3)_n$ ammonia-wire clusters: an overview

3.1. *Structures and electronic origins*

We have investigated the 7HQ·$(NH_3)_n$, $n = 1$–4 clusters in the ground and first excited states with the B3LYP density functional and the 6-311++G(d,p) basis set. Figure 7 shows the energetically lowest structures. The minimum energy structure of 7HQ·NH_3 is C_s symmetric in both the S_0 and S_1 states. Both the *trans*- and *cis*-rotamer of 7HQ are observed in the molecular-beam environment [70, 75]; the more stable *cis*-rotamer is shown in figure 7 while the *trans*-rotamer is 1.6 kcal/mol less stable.

The most stable structure of 7HQ·$(NH_3)_2$ is also C_s symmetric with the H-bond network of the ammonia wire coplanar to the aromatic frame. The *trans*- and *cis*-rotamer homodromic cyclic isomers with H-bonds from the second NH_3 back to the O–H group are 2.5 and 1.6 kcal/mol less stable than the *cis*-ammonia wire isomer.

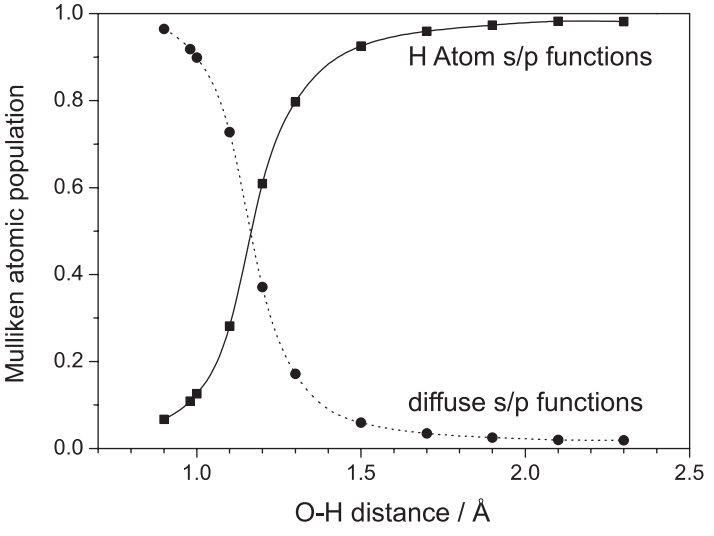

Figure 6. Mulliken atomic populations of the σ^* orbital for the dummy centre (dotted) and for the O–H hydrogen atom (solid) in the $\pi\sigma^*$ state.

For $7HQ \cdot (NH_3)_3$, an extensive search yielded only three energetically low-lying isomers. These have been labelled as in [75]: *3ch3* is the ammonia wire isomer, *3cy3* involves a cycle from the O–H group back to the O-atom and *3ch2cy2* involves a chain of two and a cycle of two ammonia molecules, one molecule joining both structures. The *3ch3* isomer is calculated to lie 1.2 kcal/mol below *3cy3* and 1.8 kcal/mol below *3ch2cy2*. We expect the populations of the *3cy3* and *3ch2cy2* isomers to be small at the supersonic jet temperatures of $\approx$10 K.

For the $7HQ \cdot (NH_3)_4$ clusters, we investigated four isomers using the same nomenclature: *4ch4*, *4ch3cy2*, *4ch2cy3* (not shown in figure 7), and *4bch3* involving a bifurcated chain. The B3LYP calculations predict small energy differences of $<$0.7 kcal/mol between these isomers, thus, we expect several isomers to be present in the supersonic expansion, in agreement with our experimental observations (see below).

The stability order of the isomers predicted by the B3LYP calculations are independently confirmed by comparisons of the experimentally observed 0_0^0 origins with the theoretical excitation frequencies. The latter were calculated by time-dependent density functional theory (TD-DFT) using the B3LYP functional and the 6-311++G(d,p) basis set, as for the binding energy calculations. Figure 8 plots the calculated excitation energies vs. the experimental 0_0^0 bands [74, 76–78]. The correlation between the TD-B3LYP calculated and experimentally observed electronic origins is very good. In absolute terms, the calculated transition energies are only 6–7% higher than experiment. The electronic origins of the clusters $7HQ \cdot (NH_3)_n$, with $n = 0$–2 and $7HQ \cdot (H_2O)_n$ with $n = 1$–3 are used as reference points to fit the curve in figure 8. The slight curvature can be rationalized by taking into account that (i) the experimental excitations are *adiabatic* while the calculated excitations from the S_0 state structures are vertical; (ii) the vertical excitation from the ground state equilibrium geometry occurs to

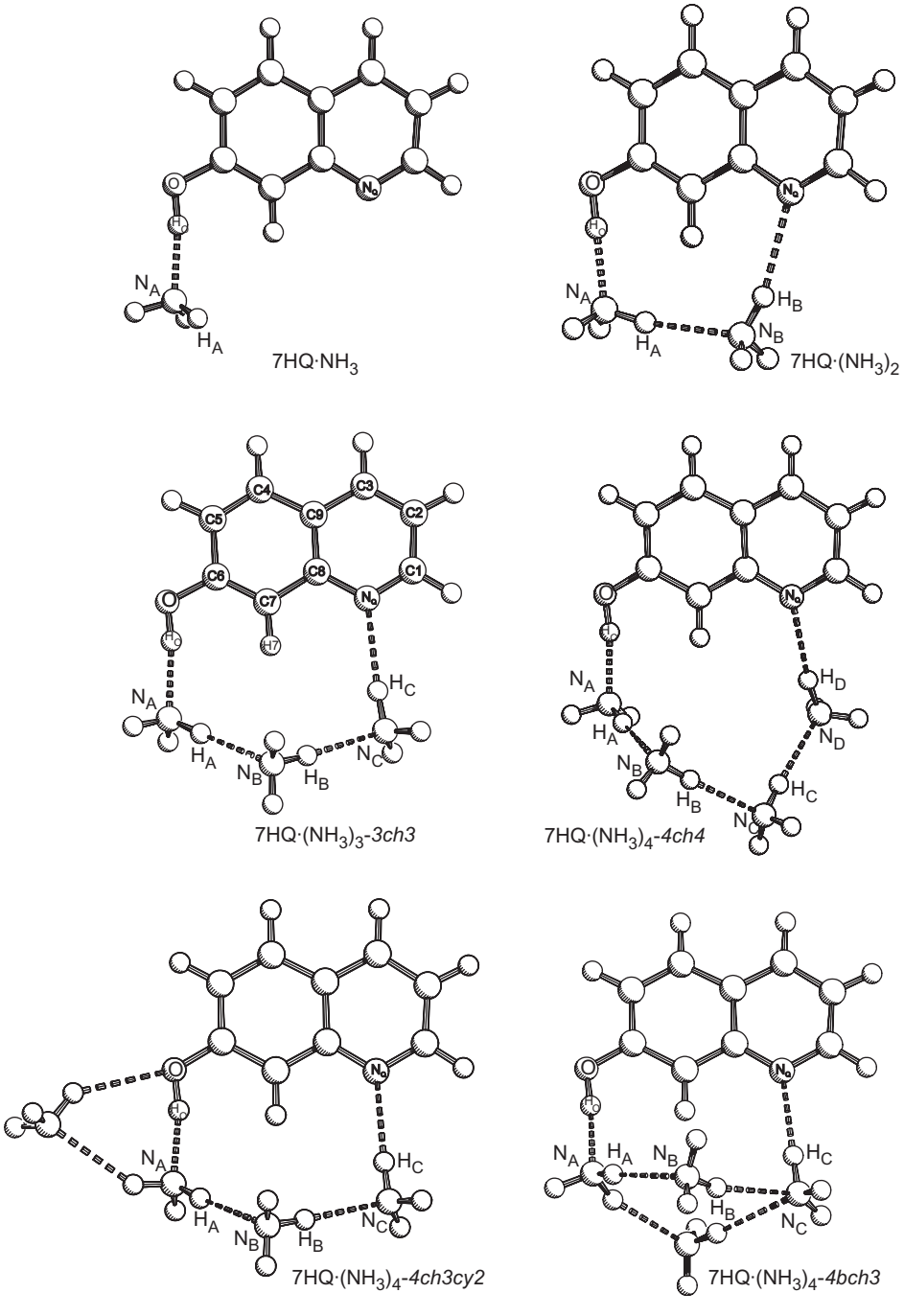

Figure 7. Minimum-energy structures of 7-hydroxyquinoline · $(NH_3)_n$ clusters with $1 \leq n \leq 4$.

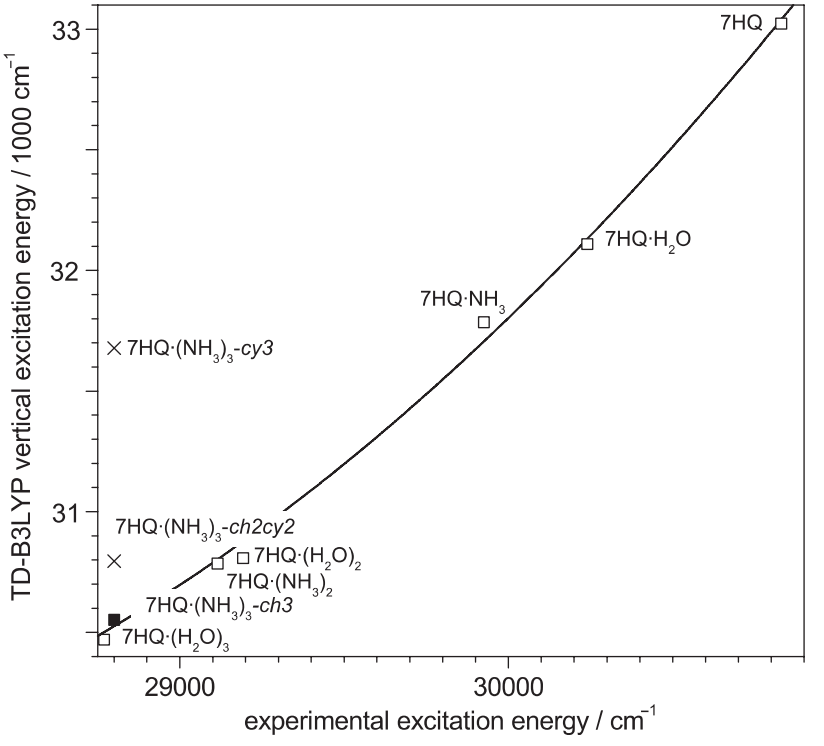

Figure 8. The calculated time-dependent B3LYP $S_1 \leftarrow S_0$ frequencies vs. experimental 0_0^0 frequencies of 7HQ, $7HQ \cdot (NH_3)_n$ ($1 \leq n \leq 3$) and the $7HQ \cdot (H_2O)_n$ ($1 \leq n \leq 3$) clusters. The values indicated by □ are used for the parabolic fit. The $7HQ \cdot (NH_3)_3$ isomers marked by × are not observed experimentally.

a non-relaxed excited-state geometry and the extent of relaxation is expected to increase with cluster size.

For the *3ch3* ammonia-wire isomer cluster, the TD-B3LYP predicted origin frequency is in nearly perfect agreement with experiment. The electronic origins of the *3ch2cy2* and *3cy3* isomers are predicted to lie 225 cm^{-1} and 1100 cm^{-1} to the blue of the *3ch3* isomer, indicated in figure 8. Indeed, no signals have been observed for these less stable isomers.

3.2. *Resonant two-photon ionization spectra*

The $7HQ \cdot (NH_3)_n$ clusters were synthesized and cooled in a 20 Hz pulsed supersonic expansion of Ne mixed with 0.3–1% NH_3. Two-colour resonant two-photon ionization (2C-R2PI) spectra were measured by crossing the jet with excitation and ionization laser beams in the source of a time-of-flight mass spectrometer. The ionization laser was tuned above the onset of two-colour photoion signal. The experimental details are described elsewhere [79, 80].

Figure 9 shows the $S_1 \leftarrow S_0$ 2C-R2PI spectra of the $7HQ \cdot (NH_3)_n$ clusters with $1 \leq n \leq 4$. Up to $n = 3$, the spectra show discrete and narrow bands with rotational

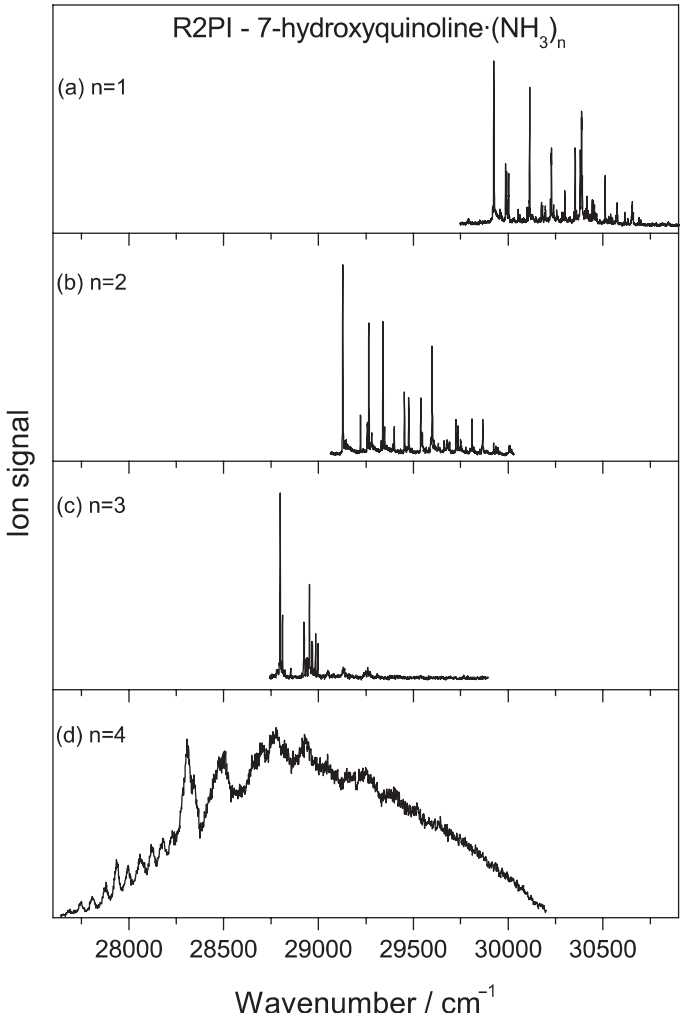

Figure 9. Two-colour resonant two-photon ionization spectra of 7-hydroxyquinoline $\cdot (NH_3)_n$, $1 \leq n \leq 4$.

contours of 1–2 cm^{-1} width. The $n = 1$ spectrum exhibits sharp bands from 29 900 cm^{-1} to $>1500\,cm^{-1}$ higher and the $n = 2$ spectrum from 29 100 to $>900\,cm^{-1}$ higher frequencies [74, 78]. In contrast, the $n = 3$ spectrum abruptly falls off $\sim 200\,cm^{-1}$ above the $S_1 \leftarrow S_0$ electronic origin. This disappearance is due to the onset of a fast process at $\sim 200\,cm^{-1}$ excess vibrational energy. As discussed below, this process has been identified as excited state H-atom transfer along the ammonia chain, ultimately resulting in the enol $\rightarrow$ keto tautomerization [81]. For $7HQ \cdot (NH_3)_4$, bands with much larger widths of 25–70 cm^{-1} are observed, which are superimposed on a continuous background. Bach *et al.* have concluded that the discrete but broad bands at lower frequencies and loss of vibrational structure at higher frequencies are due to ultrarapid excited-state processes such as H-atom transfer [77].

4. Excited-state hydrogen atom transfer in 7-hydroxyquinoline·$(NH_3)_3$

4.1. *UV–UV depletion and fluorescence action spectra*

Figure 10(a) shows the low-frequency part of the $S_1 \leftarrow S_0$ 2C-R2PI spectrum of $7HQ \cdot (NH_3)_3$ in more detail: About 200 cm^{-1} above the origin, the narrow vibronic bands disappear, with traces of band structure at +256 and +332 cm^{-1}. The UV–UV depletion spectrum in figure 10(b) is a three-laser experiment: The two lasers for the 2C-R2PI measurement are fixed at the electronic origin and monitor the constant vibronic ground state population of the cluster. A third hole-burning laser is fired ~100 ns before the 2C-R2PI measurement. If it is tuned to the $S_1 \leftarrow S_0$ electronic

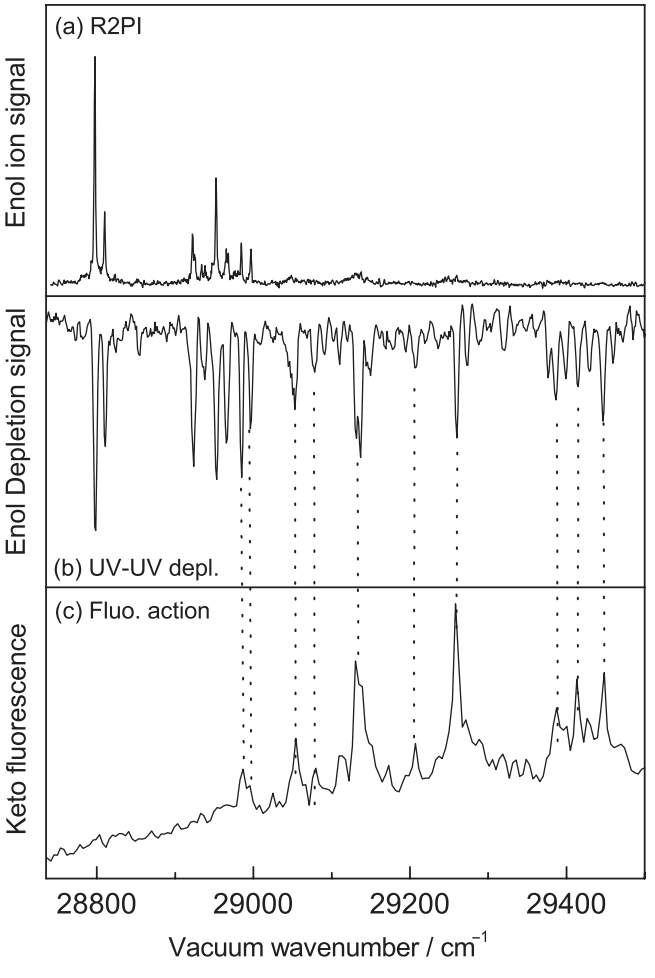

Figure 10. Spectra of $7HQ \cdot (NH_3)_3$ in the excited state by three different techniques: (a) two-colour resonant two-photon ionization spectrum of $7HQ \cdot (NH_3)_3$, (b) UV–UV depletion spectrum of $7HQ \cdot (NH_3)_3$, and (c) fluorescence action spectrum of $7HQ \cdot (NH_3)_3$ at 18 360 cm^{-1}.

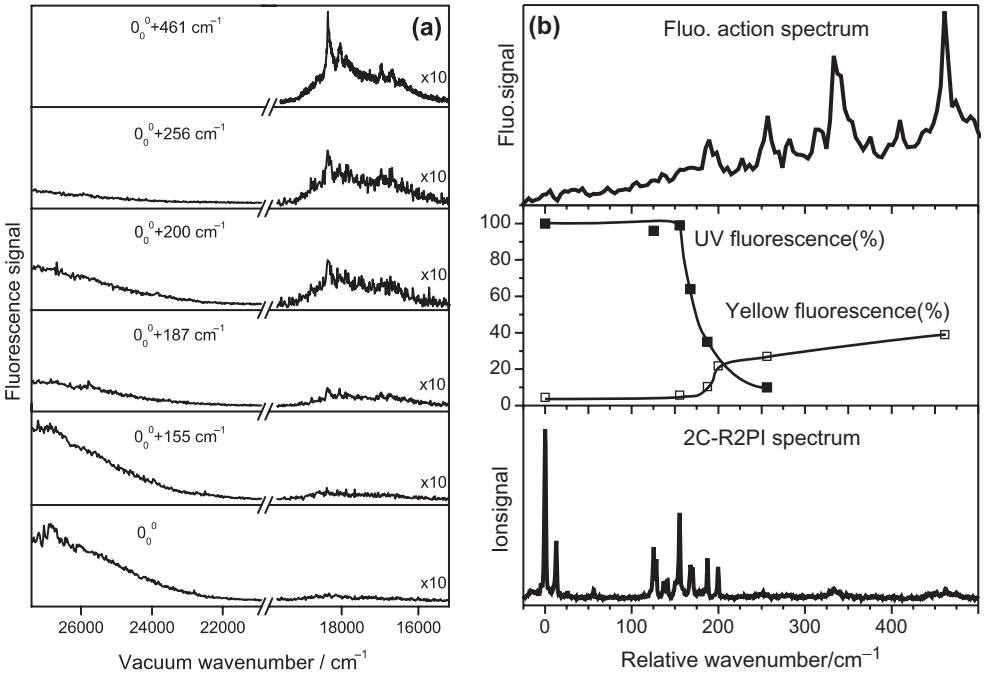

Figure 11. (a) UV-visible fluorescence spectra of 7-hydroxyquinoline$\cdot(NH_3)_3$, excited at the 0_0^0, +155, +187, +200, +256 and +461 cm^{-1} bands. The visible fluorescence spectra are scaled 10×. The UV fluorescence from the +461 cm^{-1} band cannot be measured due to the fluorescence from the $n=2$ cluster. (b) Top: keto fluorescence action spectrum. center: The integrated UV and yellow fluorescence intensities, cf. part (a), as a function of the vibrational excitation energy. The UV fluorescence from the 0_0^0 band is set to 100. Bottom: 2C-R2PI spectrum of 7HQ$\cdot(NH_3)_3$.

origin, the ground-state population is depleted, and the resulting 'dip' is observed in the 2C-R2PI signal. If the hole-burning laser is scanned, a dip is observed in the R2PI signal at every vibronic band of the $S_1 \leftarrow S_0$ spectrum. The depletion of the ground state population is proportional to the Franck–Condon factor as in the R2PI spectrum, so the hole-burning spectrum is an approximate mirror-image of the R2PI spectrum. The hole-burning spectrum exhibits resonant dips for *all* $S_1 \leftarrow S_0$ vibronic transitions, even if the excited-state levels are very rapidly depopulated, e.g. by proton transfer, H-atom transfer or other reactions. Hence the hole-burning technique shows bands that are not observable in the R2PI spectrum.

Measurements of single vibronic level UV fluorescence from the individual vibronic bands of 7-hydroxyquinoline$\cdot(NH_3)_3$ in figure 10(a) are shown in figure 11. For these measurements, the UV laser pulse (500 μJ) crossed the jet 5 mm downstream from the nozzle. The fluorescence is dispersed with monochromator and detected with a photomultiplier. The spectra were corrected for the wavelength dependence of the monochromator transmission and the photomultiplier sensitivity curve.

The excitation of the $S_1 \rightarrow S_0$ emission of 7HQ$\cdot(NH_3)_3$ at different vibronic bands in the 0–200 cm^{-1} region leads to UV fluorescence with a lifetime of $\tau_{fl} \approx 1$ ns.

As figure 11 shows, the UV fluorescence drops off rapidly $>200\,cm^{-1}$ above the origin, in qualitative agreement with the disappearance of the 2C-R2PI signals and confirming the loss of the excited state enol $7HQ^* \cdot (NH_3)_3$ population. Concurrent with the loss of the UV fluorescence of $7HQ^* \cdot (NH_3)_3$, one observed an increase in the yellow fluorescence emission [82]. The yellow fluorescence is assigned to the S_1 state 7-ketoquinoline ($7KQ^*$) tautomer, based on extensive observation in bulk protic solvents [42–44, 49].

The fluorescence action spectrum, figure 10(c), was measured by monitoring the yellow fluorescence of the keto $7KQ \cdot (NH_3)_3$ at $18\,360\,cm^{-1}$ while scanning the excitation laser over the UV absorption bands of the enol form. This spectrum exhibits the same characteristic vibronic band pattern of $7HQ \cdot (NH_3)_3$ observed in the UV–UV depletion spectrum, which implies that excitation of the enol $7HQ \cdot (NH_3)_3$ at all energies higher than $200\,cm^{-1}$ above its origin leads to emission from the keto $7KQ^* \cdot (NH_3)_3$ cluster. Significantly, the onset of discrete bands in the action spectrum coincide with the *highest frequency* bands observed in the 2C-R2PI spectrum $\sim 200\,cm^{-1}$ above the origin. The background signal arises from fluorescence of larger clusters that are produced in the supersonic expansion; these do not show discrete bands in their 2C-R2PI spectra [76]. The excited state enol $\rightarrow$ keto tautomerization must involve excited state H^+ or H-atom translocation along the $(NH_3)_3$ wire to the quinolinic N-atom.

4.2. *Two reaction paths: ESHAT vs. ESPT*

We interpret the experimental results shown above using configuration interaction singles (CIS) calculations of the low-lying excited states. We assume that the observed excited state enol $\rightarrow$ keto tautomerization involves either proton or H-atom Grotthus-type translocation along the $(NH_3)_3$ wire to the quinolinic N-atom [81, 83]. The CIS potential energy curves for proton and H-atom transfer are shown in figure 12. For H-atom transfer, we find three local minima with an H-atom successively localized on the first, second and third ammonia molecule, cf. figure 13. These structures are denoted HT1, HT2 and HT3. The first transition state (TS) between the enol and HT1 minima is labelled $TS_{e/1}$, followed by the intermediate transition states $TS_{1/2}$ and $TS_{2/3}$. The last transition state $TS_{3/k}$ leads to the excited-state keto cluster.

The calculations predict that the $S_1 \leftarrow S_0$ excitation occurs dominantly from the highest occupied π molecular orbital (MO) on 7HQ. The enol S_1 state is a $\pi\pi^*$ excitation localized on 7HQ. On the other hand, the S_4 state is a $\pi\sigma^*$ Rydberg-type excitation. The S_1 and S_4 states cross along the H-atom transfer reaction path between the enol and the HT1-form; in C_s symmetry this leads to a conical intersection, cf. section 2.2. For non-planar geometries, such an intersection leads to an avoided crossing. Thus, the $TS_{e/1}$ barrier predicted by the CIS calculations originates from the crossing of the $\pi\pi^*$ and $\pi\sigma^*$ states, which gives rise to a non-adiabatic change of the excited state wavefunction in the vicinity of $TS_{e/1}$. The last barrier $TS_{3/k}$ originates from a reverse crossing between the $\pi\pi^*$ and $\pi\sigma^*$ states, leading to the $\pi\pi^*$ excited $7KQ^*$ tautomer.

Excited state hydrogen transfer has been modelled for phenol, indole, 1-naphthol $\cdot (NH_3)_n$ and phenol $\cdot (NH_3)_n$ clusters [63, 64, 84–86], for which the lowest $\pi\sigma^*$ excited states are dissociative along the N–H or O–H bond stretching coordinates.

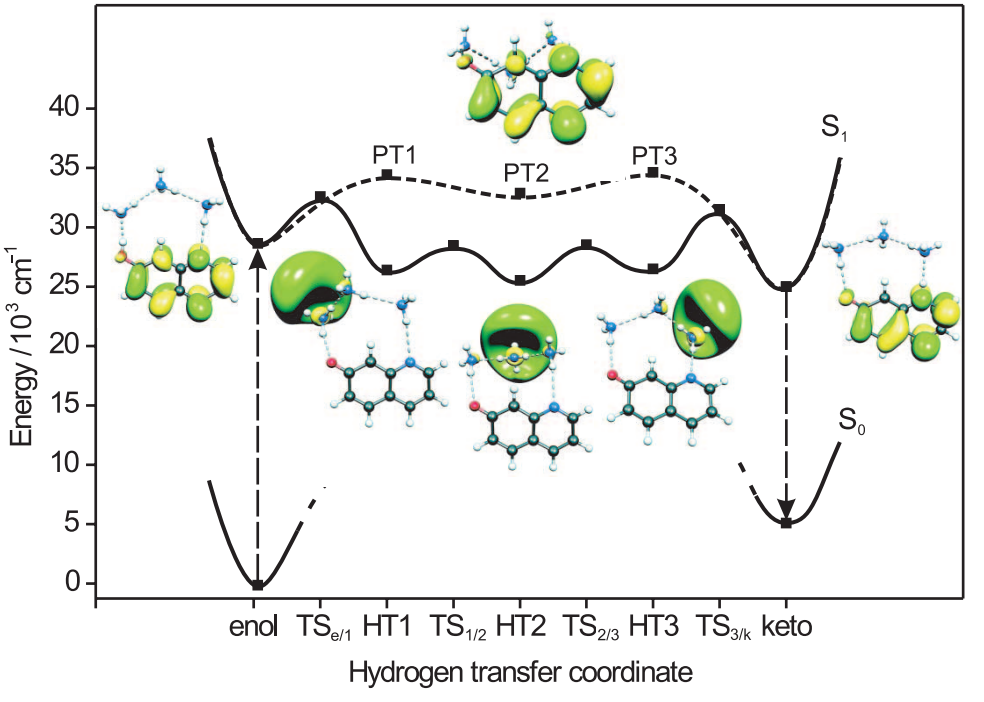

Figure 12. CIS calculated reaction profiles for the excited state H-atom transfer (full curve) and proton transfer path (dashed curve) of 7HQ · $(NH_3)_3$. The calculated energies of the enol and the keto form in the S_0 ground state are also indicated. The MOs contributing dominantly to the excited state wavefunctions are shown for the minima along the ESHAT and ESPT profiles. The S_0 state enol energy is set to zero and the S_1 state minimum of the enol is offset to match the experimental electronic origin.

Here, the $\pi\sigma^*$ state does not primarily lead to cluster dissociation but to H-atom transfers from the hydrogen-bonded O–H of 7HQ along the hydrogen-bonded $(NH_3)_3$ wire.

The calculated electronic $TS_{e/1}$ barrier height is 3720 cm^{-1}; this value should be regarded as an upper estimate since CIS typically overestimates such barriers [60, 63, 64]. These calculations predict the enol → HT1 step to be exoergic by about 2600 cm^{-1}, providing the driving force of the reaction. The HT1, HT2, HT3, and 7KQ forms lie close in energy, with the 7KQ form the lowest. Once the system passes through the $TS_{e/1}$ barrier, the two subsequent barriers are surmounted. Presumably, the H-atom fluctuates over large distances between the HT1 and HT3 forms. The last barrier $TS_{3/k}$ between the HT3 and 7KQ forms is calculated to be nearly as high as $TS_{e/1}$ and it must also be passed by tunnelling (as above, note the overestimate of barrier heights by the CIS method [60, 63, 64]).

The entire enol → keto reaction is exoergic by 3860 cm^{-1}. The calculated $S_1 \leftrightarrow S_0$ energy difference for the 7-ketoquinoline is 18 020 cm^{-1}, in good agreement with experimental fluorescence maximum at 18 360 cm^{-1}. At the CIS level, the calculated energy to remove one NH_3 molecule from the wire is about the same as that available from the exoergicity of the H transfer reaction. Hence, the enol → keto reaction may lead to loss of one NH_3 molecule from the cluster preceding the keto fluorescence.

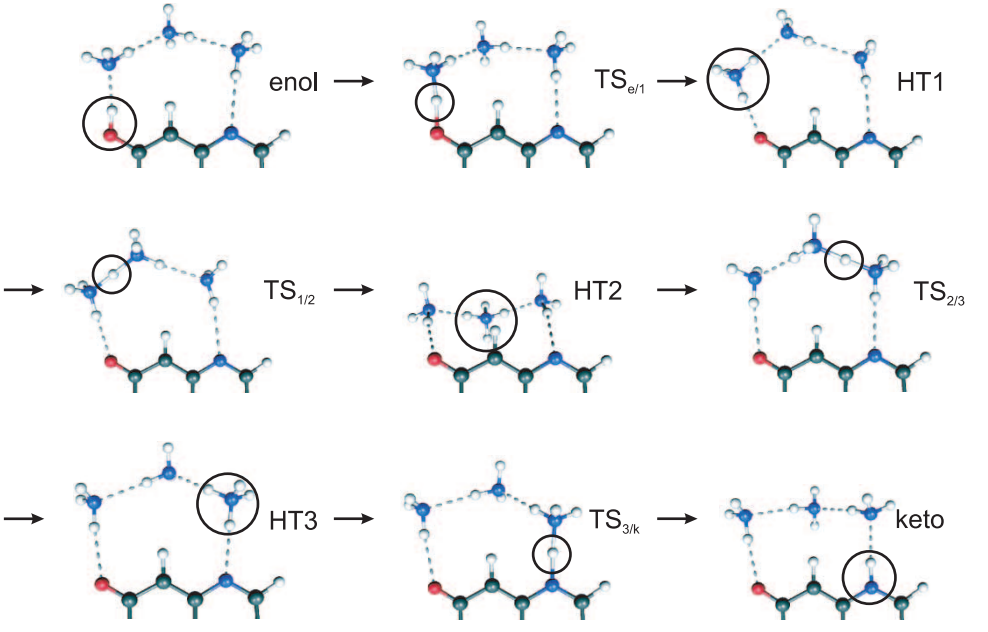

Figure 13. 7HQ·$(NH_3)_3$ structures at the stationary points along the H-atom transfer pathway, cf. figure 12. Note that the lower half of the 7HQ molecule has been cut away for increased detail.

The dominant configuration in the excited wavefunction involves promotion of an electron from the highest occupied π orbital of 7HQ to the orbitals shown in figure 12 at different steps of the reaction. For the enol, this is the 7HQ π^* orbital, but for HT1 it is a σ^* orbital on the newly generated NH_4 moiety. Accompanying this change of excited state character is a transfer of about 0.9 electrons from the 7HQ moiety to the first NH_3; i.e. the incipient proton transfer becomes an H-atom transfer in the vicinity of $TS_{e/1}$. After passing the $TS_{e/1}$ barrier, the lowest excited state retains the $\pi\sigma^*$ character along the translocation coordinate up to $TS_{3/k}$. The σ^* orbital accompanies the H-atom as it moves along the ammonia wire via HT1, HT2, and HT3, see figure 12. A reverse switch from the NH_4 σ^* to a π^* orbital on 7-ketoquinoline occurs near the $TS_{3/k}$ barrier.

Both the $\pi^* \rightarrow \sigma^*$ and the $\sigma^* \rightarrow \pi^*$ crossings lead to large changes of the $S_1 \rightarrow S_0$ oscillator strength. In C_s symmetry, fluorescence is allowed from the $\pi\pi^*$ but forbidden from the $\pi\sigma^*$ state and this selection rule is approximately retained in C_1 symmetry. The calculated $S_1 \rightarrow S_0$ oscillator strength of the 7KQ $\pi\pi^*$ state is $f = 0.294$, whereas for the $\pi\sigma^*$-type states of HT1–HT3 they are $f = 0.001$ to 0.004. This implies that the HT1–HT3 biradicals have long radiative lifetimes and explains why no fluorescence is experimentally observed from these reaction intermediates.

CASSCF calculations were then performed for the enol, HT1, HT2, HT3, and 7KQ minima and the $TS_{1/2}$ and $TS_{2/3}$ transition states, all in C_s symmetry. In C_s symmetry, the $TS_{e/1}$ and $TS_{3/k}$ transition states are conical intersections, where the transition-state

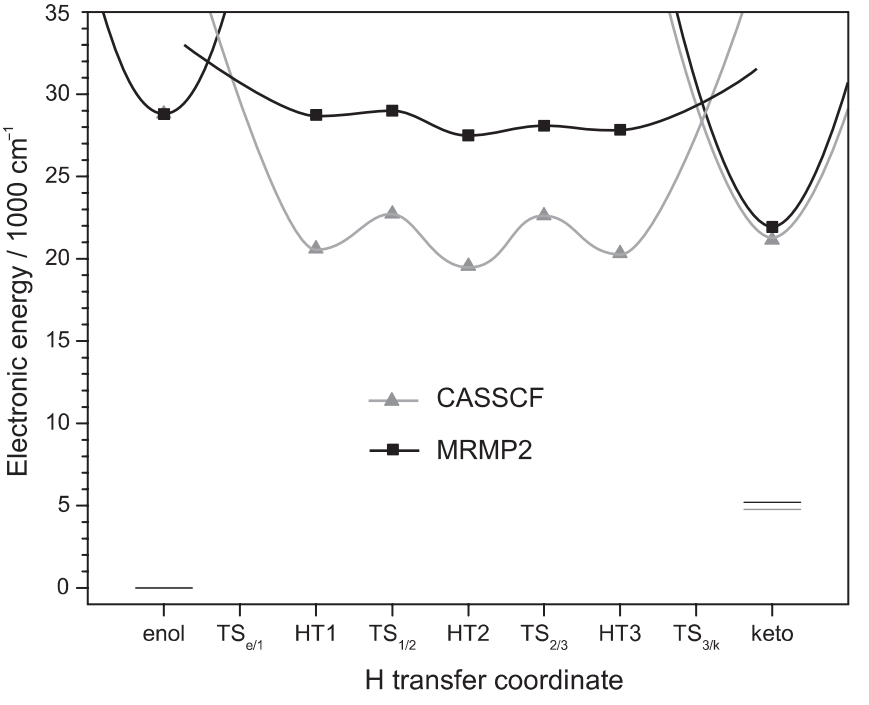

Figure 14. Calculated CASSCF (grey curve) and MRMP2 (black curve) potentials of the excited state enol → keto H-atom transfer pathway of 7HQ·$(NH_3)_3$.

optimization methods fail. For this reason, the respective energies were not calculated at the CASSCF and MRMP2 levels.

The CASSCF energies are lower than the CIS energies due to the contributions of double and higher excitations. The 7KQ form is 3800 cm^{-1} lower than at the CIS level. Also, the $\pi\sigma^*$ part of the reaction profile (HT1–HT3) is significantly stabilized relative to the $\pi\pi^*$ excited enol and keto forms. This can be rationalized by the biradical nature of this intermediate region. CASSCF calculations mainly recover the non-dynamical correlation energy and therefore the closed-shell singlets (enol and keto) are predicted too high in energy. Although at the CASSCF level the $\pi\sigma^*$ part of the reaction path from HT1–HT3 is about 10% lower than at the CIS level, the relative energies and barrier heights are very similar.

With the MRMP2 method, the calculated adiabatic transition energy for the enol is 29 245 cm^{-1}, only 450 cm^{-1} higher than the experimental 0_0^0 band. For the keto cluster the adiabatic transition energy is 17 180 cm^{-1}, 1200 cm^{-1} lower than the observed keto fluorescence maximum. The inclusion of dynamic correlation at the MRMP2 level has impressive effects relative to the CASSCF calculations. The $\pi\sigma^*$ part of the reaction profile (HT1–HT3) is moved upward into the vicinity of the CIS energies. Furthermore, the barriers at $TS_{1/2}$ and $TS_{2/3}$ are lowered relative to both the CIS and CASSCF calculations.

The existence and energetics of the excited state *proton*-transfer (ESPT) paths and structures have not been addressed in previous investigations of excited-state HAT reactions [59, 62–64]. We studied the ESPT pathway of $7HQ\cdot(NH_3)_3$ at the CIS level. Starting with the HT1, HT2, and HT3 equilibrium structures, the systems were held in the $\pi\pi^*$ state and optimizations were performed. As shown in figure 12, the resulting ESPT pathway exhibits a single minimum; since its structure is analogous to HT2, it is denoted PT2. The proton transferred forms analogous to HT1 and HT3 are transition states that lie ~16 kcal/mol above the enol, cf. figure 12; they are denoted PT1 and PT3. The enol → PT2 reaction corresponds to a *synchronous* translocation of the two protons from O → N_1 and from N_1 → N_2. The PT1 barrier is 5.2 kcal/mol higher than the $TS_{e/1}$ H-atom transfer barrier and is much wider. The PT2 minimum is 11.7 kcal/mol less stable than the enol. Consequently, the $S_1 \leftarrow S_0$ electronic excitation provides no driving force for the ESPT reaction. There is no competition between PT and HAT in the excited state. That the $\pi\pi^*$ state reaction involves a proton transfer is shown by Mulliken population analysis: In the $\pi\pi^*$ PT2 form, the NH_4 moiety carries a Mulliken charge of $+0.70e$, whereas it is $-0.41e$ in the $\pi\sigma^*$ state. In other words, the charge difference between the two forms is ~1. To summarize: the dominant orbital character of the lowest excited state of the intermediate forms determines whether the reaction is a proton transfer (the system stays on the $\pi\pi^*$ state surface) or a H-atom transfer (the intermediate forms are in a low-lying $\pi\sigma^*$ state).

4.3. *The enol → HT1 reaction coordinate*

The intrinsic reaction coordinate (IRC) for the enol → HT1 step of the H-atom transfer reaction was calculated at the CIS/6-31(+)G(d,p) level. The IRC is the steepest descent path in mass-weighted coordinates and is calculated by propagating the system from the transition state $TS_{e/1}$ backwards and forwards towards the enol and HT1 minima.

The enol → HT1 reaction profile in figure 15 is plotted as a function of the 'heavy' coordinate O···N_A and of the 'light' coordinate σ, which mainly involves H-atom motion. It is defined as the difference (O···P) – (P···N_A), where P is the projection of the H-atom on the O···N_A axis. The projection of the IRC onto the potential energy vs. σ plane in figure 15 is similar to the curve obtained if the O–H distance is used as a driving coordinate [87]. The other two projections (energy vs. O···N and O···N vs. σ) show the utility of the 'light' and a 'heavy' coordinates: the reaction starts at the enol minimum with $R = 2.80$ Å and $\sigma = -0.87$ Å. In a first step, both R and σ contract by ~0.35 Å and the potential energy rises by ~1500 cm^{-1}. In a second phase, the O···N_A distance remains constant at 2.47 Å whereas σ increases from −0.5 to +0.44 Å; this part of the reaction accounts for 60% of the barrier height (2300 cm^{-1} out of 3800 cm^{-1}). In the last phase, R increases by about 0.45 Å and σ by 0.3 Å. Most of the barrier is passed along the H-atom transfer coordinate, implying that tunnelling is very important for this reaction.

4.4. *Vibrational mode selectivity*

For the $7HQ\cdot(NH_3)_3$ cluster, all overtones and combinations of the *intermolecular* ammonia-wire vibrations appear only in the UV–UV depletion spectrum but not in

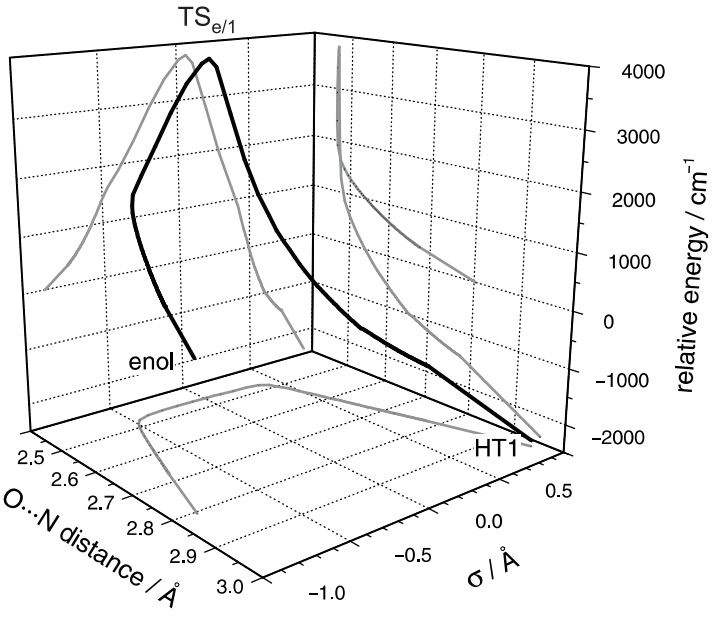

Figure 15. Intrinsic reaction coordinate (IRC) connecting the enol and HT1 minima. The potential energy is plotted against the 'heavy' O···N coordinate and the 'light' σ coordinate, see text.

the R2PI spectrum. However, several intramolecular vibrational fundamentals are weakly observed in the R2PI spectrum *above* the threshold [80], see figure 9. This implies that the intramolecular vibrations accelerate the ESHAT reaction less efficiently than the intermolecular modes. This mode selectivity is especially pronounced for the deuterated cluster d_2-7DQ · $(ND_3)_3$, for which intramolecular vibronic bands appear in the R2PI spectrum quite far above the 300 cm^{-1} reaction threshold, see figure 16.

Within the framework of non-adiabatic proton transfer theory, several models have been developed that predict a vibrational state dependence of the tunnelling rates [4, 9, 88–92]. Based on these concepts, one expects that excitation of the intermolecular ammonia-wire stretching modes allow the cluster to approach $TS_{e/1}$, thereby increasing the tunnelling rate.

Figure 17 shows the normal mode eigenvectors that correspond to the strongest vibronic excitations of the $S_1 \leftarrow S_0$ transition. The detailed analyses and mode assignments for 7HQ · $(NH_3)_3$ and 7DQ · $(ND_3)_3$ are given in [80]. Briefly, the vibrations can be grouped into the *inter*molecular modes δ_1 (out-of-plane ammonia wire deformation), σ_1 (N_C–H···N_Q stretch), σ_2 (symmetric N_A–H···N_B–H···N_C–H stretch), σ_3 (antisymmetric N_A–H···N_B–H···N_C–H stretch) and σ_4 (O–H···N_A stretch). The σ_3 mode is mixed with the intramolecular out-of-plane deformation ν_2 and is denoted ν_2/σ_3 below. The ν_4, ν_7, and ν_{14} modes are dominantly in-plane intramolecular vibrations of 7HQ.

Intermolecular vibrations with components along the 7HQ–O–H···NH_3 hydrogen bond distance directly modulate the tunnelling path for the ESHAT reaction, cf. section 4.3. On the other hand, excitation of *intra*molecular vibrations distorts the

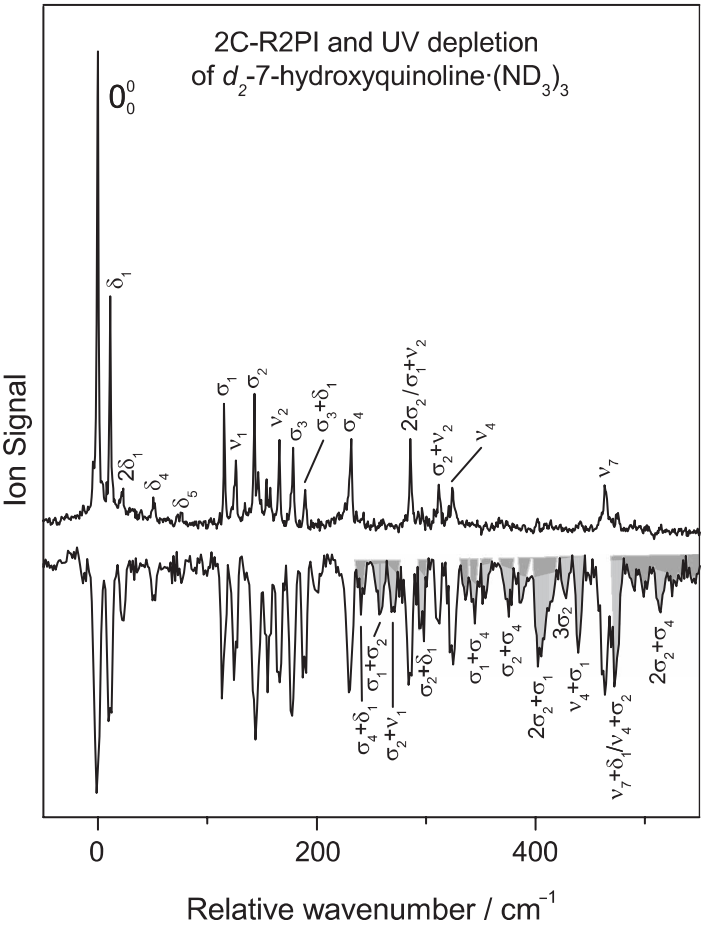

Figure 16. 2C-R2PI and UV–UV depletion spectra of the deuterated cluster d_2-7DQ·$(ND_3)_3$. The bands indicated in grey in UV–UV depletion are not observed in the 2C-R2PI spectrum.

7-hydroxyquinoline framework but typically does not drive the system toward the $TS_{e/1}$ barrier [80]. The mode selectivity is closely connected to the $\pi\pi^*/\pi\sigma^*$ state crossing: the modes that accelerate the ESHAT are those that *reduce the energy difference* between the $\pi\pi^*$ and the $\pi\sigma^*$ states. For each vibrational mode, the $\pi\pi^*$ and $\pi\sigma^*$ potential energy curves were calculated for small displacements along the $\pi\pi^*$ state normal-mode eigenvectors. Figure 18 shows the resulting curves for the σ_1, σ_2, and σ_4 *inter*molecular modes and for the ν_2/σ_3, ν_4, and ν_7 *intra*molecular modes, respectively.

For the $\pi\pi^*$ state, all the potential curves are close to harmonic, albeit with different curvatures. However, for the $\pi\sigma^*$ state, displacement along the three intermolecular coordinates leads to monotonic decreases, viz. figure 18. Since the ESHAT reaction barrier is formed by the crossing of the $\pi\pi^*$ and $\pi\sigma^*$ states, displacement along these intermolecular coordinates must lead towards regions with lower barriers.

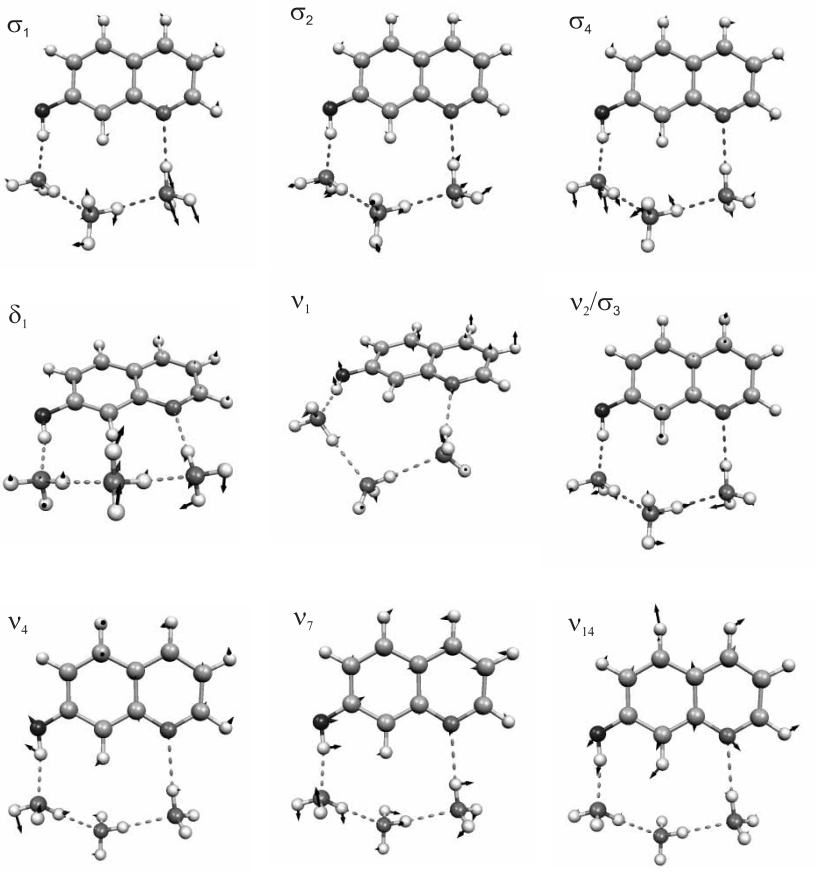

Figure 17. Low-frequency inter- and intramolecular vibrational eigenvectors of 7-hydroxyquinoline · $(NH_3)_3$. The modes for the deuterated cluster are similar.

In contrast, along the ν_2/σ_3 and ν_4 coordinates the PE curves in the $\pi\sigma^*$ state are much closer to those in the $\pi\pi^*$ state. Vibrational excitation along these coordinates does not reduce the $\pi\pi^*$-$\pi\sigma^*$ energy difference significantly. The potential energy curves of δ_1, ν_1, and ν_{14} (not shown here) are similar to those of ν_2/σ_3 and ν_4.

In order to compare the effects of the different modes on an equal footing, we chose the vibrational displacement in the $\pi\pi^*$ state to correspond to that of the respective $\pi\pi^*$ fundamental vibrational frequency. Figure 19(a) shows for 7HQ · $(NH_3)_3$ the calculated energy difference between the $\pi\pi^*$ and the $\pi\sigma^*$ states plotted against the vibrational energy in the $\pi\pi^*$ state. The energy differences are highly specific to the vibrational mode: Vibrational displacements along the intramolecular modes ν_1, ν_2/σ_3, ν_4, and ν_{14}, and the intermolecular mode δ_1 either increase (by less than 100 cm^{-1}) or do not change the $\pi\pi^*$-$\pi\sigma^*$ energy difference. Hence they will not lower the tunnelling barrier. On the other hand, the intermolecular modes σ_1, σ_2, σ_4, and the intramolecular mode ν_7 decrease the $\pi\pi^*$–$\pi\sigma^*$ energy difference by 300–450 cm^{-1}, i.e. excitation of these modes

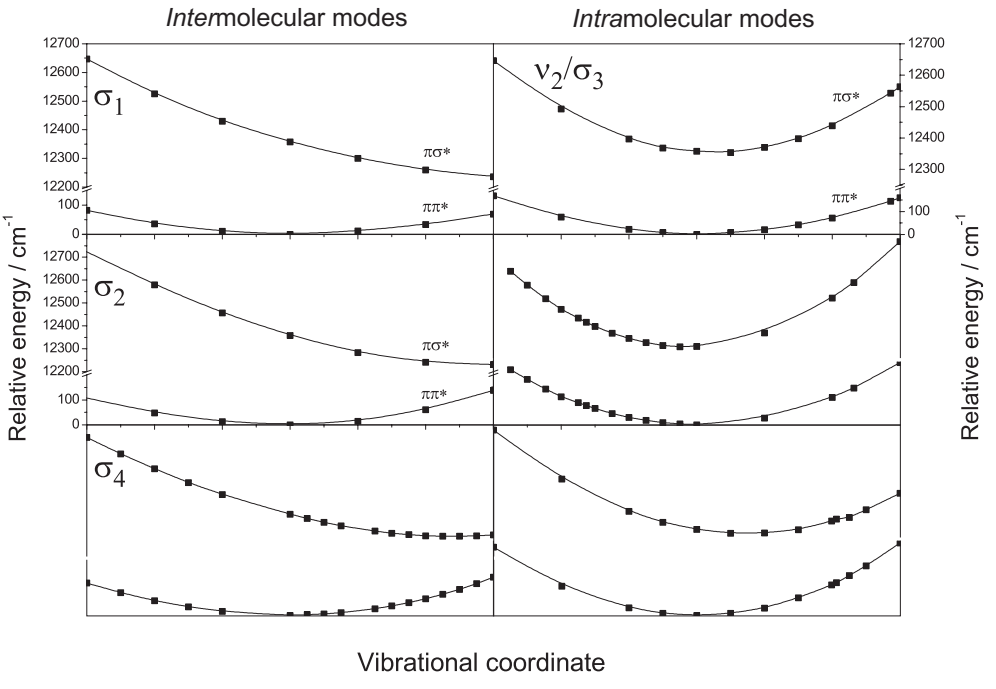

Figure 18. CIS calculated potential along the *inter*molecular normal coordinates σ_1, σ_2, and σ_4 (left) and along the *intra*molecular normal coordinates ν_2/σ_3, ν_4, and ν_7 (right), for the $\pi\pi^*$ and the $\pi\sigma^*$ states. Note the break in the vertical energy scale.

in the $\pi\pi^*$ state leads to considerable decreases of the barrier height. Similar effects are predicted for the deuterated cluster, shown in figure 19(b).

The calculated mode-selective effects as well as the changes in mode selectivity upon deuteration are in good agreement with the experimental results. For $7HQ \cdot (NH_3)_3$ the three stretching fundamentals σ'_1, σ'_2 and σ'_3 are observed in the R2PI spectrum, while σ'_4 lies above the reaction threshold and is only observable in the UV–UV depletion spectrum. All combinations and overtones of σ'_1, σ'_2, σ'_3 and σ'_4 have very short lifetimes and do not appear in the R2PI spectrum. The intramolecular vibrations ν_4 and ν_7 are weakly observed in the 2C-R2PI spectrum.

For $7DQ \cdot (ND_3)_3$, the disappearance of the vibronic bands in the R2PI spectra sets in around $300\,cm^{-1}$, see figure 16. Also, the threshold is not sharp and several vibronic levels appear around $300\,cm^{-1}$; e.g. $2\sigma'_2$, $\sigma'_2 + \nu'_2$ and ν'_4. The intramolecular mode ν'_7 appears more intensely in the R2PI spectrum than for the non-deuterated cluster and the ν'_{14} mode is detectable, while the UV–UV depletion spectrum shows a number of intermolecular overtone and combination bands that do not appear in the R2PI spectrum above $300\,cm^{-1}$; e.g. the $2\sigma'_2 + \sigma'_1$ combination is only 10% lower in frequency than ν'_7 and exhibits similar intensity but only ν'_7 remains in the R2PI spectrum. This clearly shows that the mode selectivity is even stronger for the $7DQ \cdot (ND_3)_3$ cluster and that the two intramolecular modes ν'_7 and ν'_{14} accelerate the ESHAT reaction considerably less than the intermolecular vibrations.

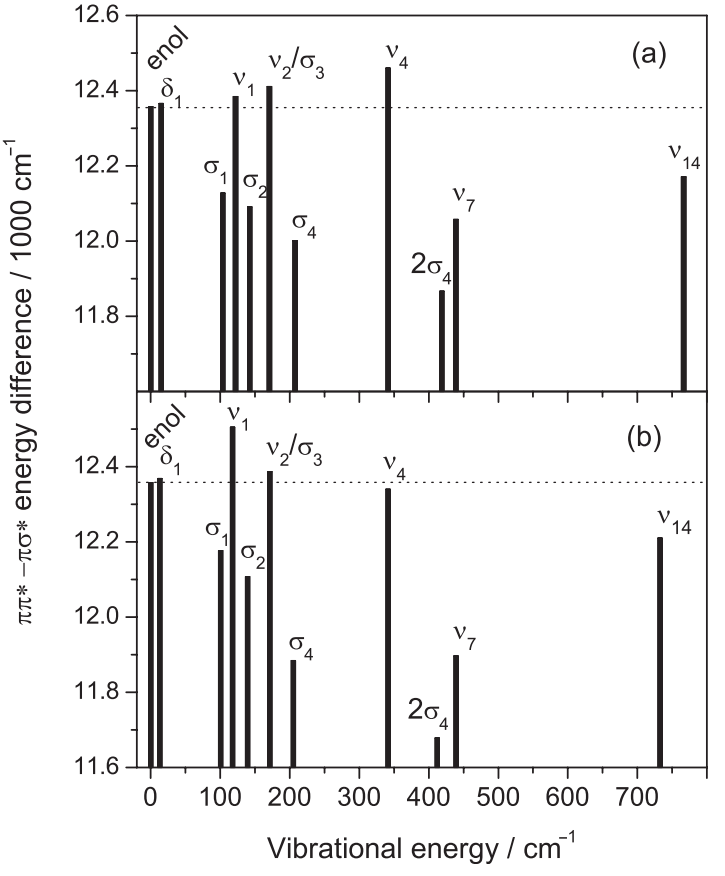

Figure 19. Calculated energy differences of the $\pi\pi^*$ and $\pi\sigma^*$ potential energy surfaces (in cm^{-1}) of the $7HQ \cdot (NH_3)_3$ (a) and $7DQ \cdot (ND_3)_3$ (b) enol clusters, plotted vs. the $v = 0 \rightarrow 1$ excitation energy. For each vibrational mode, the displacement along the positive vibrational coordinate (as shown in figure 17) is chosen to yield the vibrational $v = 0 \rightarrow 1$ excitation energy in the $\pi\pi^*$ state. The $\pi\pi^*$–$\pi\sigma^*$ vertical energy difference is calculated at this displacement.

5. Solvent effects on excited state H-atom transfer: mixed ammonia/water clusters

5.1. *Comparison of $7HQ \cdot (H_2O)_3$ and $7HQ \cdot (NH_3)_3$*

Following the description of the effects of excited-state H-atom transfer on the $S_1 \leftarrow S_0$ spectra of $7HQ \cdot (NH_3)_3$, we discuss the effects of stepwise substituting NH_3 by H_2O in the $n = 3$ solvent-wire cluster. Figure 20 shows the mass-selected two-colour R2PI spectra of $7HQ \cdot (NH_3)_3$, the $7HQ \cdot (NH_3)_n \cdot (H_2O)_m$ mixed clusters with $n + m = 3$ and the water-wire cluster $7HQ \cdot (H_2O)_3$. All spectra are plotted relative to the respective $S_1 \leftarrow S_0$ electronic origins. Figure 20(b) and (c) are hole-burning difference spectra, since the 2C-R2PI spectrum of $7HQ \cdot (NH_3)_2 \cdot H_2O$ (not shown) is a superposition of the spectra of two isomers with origins at 28 348 cm^{-1} (isomer A) and 28 694 cm^{-1}

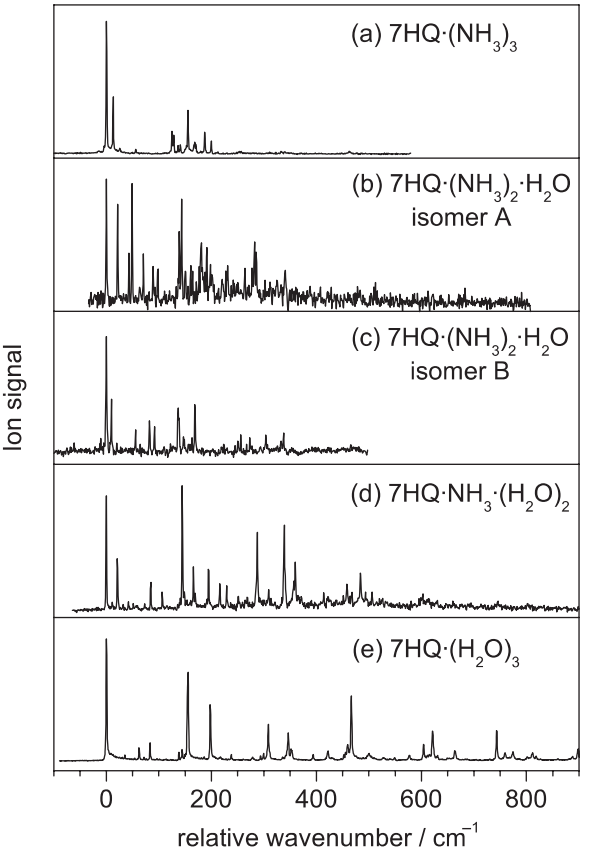

Figure 20. Two-colour resonant two-photon ionization spectra of $7HQ \cdot (NH_3)_3$ (a), $7HQ \cdot H_2O(NH_3)_2$ (b-c), $7HQ \cdot (H_2O)_2NH_3$ (d), and $7HQ \cdot (H_2O)_3$ (e).

(isomer B), respectively [93]. For $7HQ \cdot NH_3 \cdot (H_2O)_2$ and $7HQ \cdot (H_2O)_3$, hole-burning experiments show that the spectra in figure 20(d) and (e) are due to single isomers.

The band structure in figure 20(a)–(e) is seen to extend to increasingly higher vibrational frequencies with increasing H_2O content of the cluster. For $7HQ \cdot (NH_3)_3$, the structure breaks off $\sim 200\,cm^{-1}$ above the origin, for the two isomers of $7HQ \cdot (NH_3)_2 \cdot H_2O$ it breaks off at $\sim 350\,cm^{-1}$ above their respective electronic origins and for $7HQ \cdot NH_3 \cdot (H_2O)_2$ above $\sim 500\,cm^{-1}$. In contrast, the spectrum of $7HQ \cdot (H_2O)_3$ exhibits sharp vibronic bands up to $> 12\,500\,cm^{-1}$. From this, we can draw several conclusions. (i) The energy threshold for H-atom transfer depends on the chemical composition of the solvent wire. Stepwise replacement of NH_3 by H_2O increases the energy threshold for H-atom transfer. (ii) The observation of an extended R2PI spectrum for $7HQ \cdot (H_2O)_3$ shows that no excited-state reaction occurs for $7HQ \cdot (H_2O)_3$ up to an excess vibrational energy of $1500\,cm^{-1}$. (iii) The fact that the vibronic band structure of $7HQ \cdot (NH_3)_3$ and all the $7HQ \cdot (NH_3)_n \cdot (H_2O)_m$ mixed

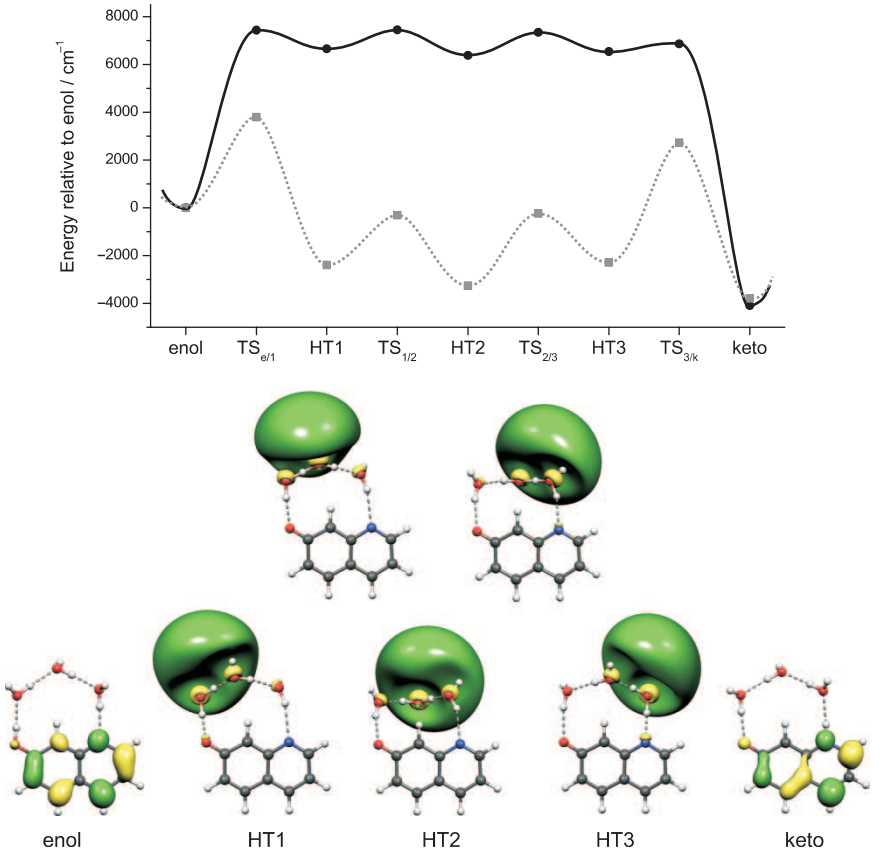

Figure 21. CIS/6-31(+)G(d,p) ESHAT reaction profiles for the water-wire 7HQ · $(H_2O)_3$ (black) and ammonia-wire 7HQ · $(NH_3)_3$ (grey). Below: Molecular orbitals contributing dominantly to the S_1 state wavefunctions for the important stationary points along the ESHAT profile for 7HQ · $(H_2O)_3$.

clusters break off in the range 200–600 cm^{-1} shows that a single NH_3 molecule in the solvent-wire induces the excited-state reactivity.

As for 7HQ · $(NH_3)_3$ above, we have analysed the effects of the composition of the solvent wire on the ESHAT reaction based on CIS/6-31(+)G(d,p) calculations. Figure 21 compares the calculated ESHAT reaction profiles of the pure water-wire and ammonia-wire clusters, 7HQ · $(H_2O)_3$ and 7HQ · $(NH_3)_3$. The profiles exhibit the same types of stationary points, the successive minima corresponding to subsequent Grotthus-like H-atom translocated structures. The first H-atom transfer along the water-wire is predicted to be strongly endoergic. Also, the HT1–HT3 intermediates for the water-wire all lie 6400–6800 cm^{-1} *above* the enol minimum, whereas for the ammonia-wire they lie 2300–3250 cm^{-1} below the enol. Figure 21 also shows the orbitals that contribute dominantly to the S_1 state wavefunctions. As for 7HQ · $(NH_3)_3$, the enol and keto tautomers of 7HQ · $(H_2O)_3$ give rise to $\pi\pi^*$ type excitations, whereas the structures HT1–HT3 and the two intermediate transition states are of $\pi\sigma^*$ type.

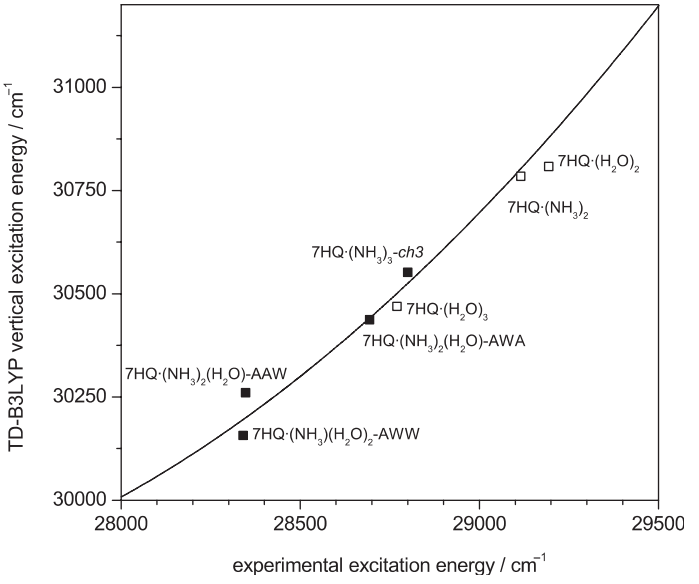

Figure 22. The calculated vertical TD-B3LYP $S_1 \leftarrow S_0$ transitions vs. experimental 0_0^0 transitions of the mixed ammonia-water clusters $7HQ \cdot (NH_3)_n \cdot (H_2O)_m$ $(n+m=3)$. The curve was fitted to the values for $7HQ \cdot (NH_3)_n$ $(n=0\text{–}2)$ and $7HQ \cdot (H_2O)_n$ $(n=1\text{–}3)$, see figure 8.

In the vicinity of the enol–HT1 barrier $TS_{e/1}$ and the HT3–keto barrier $TS_{3/k}$, strong non-adiabatic $\pi\pi^* \leftrightarrow \pi\sigma^*$ mixing occurs, and the S_1 state wavefunction cannot be described in terms of single-electron excitations.

5.2. *The mixed 7HQ·(NH$_3$)$_2$·H$_2$O and 7HQ·NH$_3$·(H$_2$O)$_2$ clusters*

The three stable isomers *3ch3*, *3ch2cy2* and *3cy3* found for $7HQ \cdot (NH_3)_3$ [80] were used to generate starting structures for the mixed clusters. All possible sequence substitutions were considered, e.g. ammonia–water–water (AWW), water–ammonia–water (WAW) and water–water–ammonia (WWA) for the $7HQ \cdot NH_3 \cdot (H_2O)_2$ cluster. The sequence substitutions of the three isomers results in nine isomers each for $7HQ \cdot (NH_3)_2 \cdot H_2O$ and $7HQ \cdot NH_3 \cdot (H_2O)_2$.

The assignment of the three spectra in figure 20 to specific structure and sequence isomers is based on the calculated H-bond binding energies, and on the calculations of the 0_0^0 transition frequencies with the TD-B3LYP method, cf. section 3.2. For the identification of the mixed cluster isomers, we extrapolate the curve of figure 8 to lower transition frequencies in figure 22. The observed $7HQ \cdot NH_3 \cdot (H_2O)_2$ electronic origin perfectly matches the calculated transition for the *3ch3*–AWW isomer, but not for the *3ch3*–WAW and *3ch3*–WWA isomers. For the two observed isomers of the $7HQ \cdot (NH_3)_2 \cdot H_2O$ cluster, very good agreement is found for isomer B with the calculated *3ch3*–AWA isomer. The $7HQ \cdot (NH_3)_2 \cdot H_2O$ isomer A is assigned as *3ch3*–AAW with a slight discrepancy, but still in good agreement with the other

clusters. These assignments agree perfectly with those obtained from the calculated relative cluster stabilities.

The calculated ESHAT reaction profile for the $7HQ \cdot (NH_3)_2 \cdot H_2O$ *3ch3*–AWA cluster is shown in figure 23. It closely follows that of $7HQ \cdot (NH_3)_3$ except for the central part. Replacement of an NH_3 molecule by H_2O pushes the potential upwards by about 6500 cm^{-1}. The HT2 form is no longer a minimum as in $7HQ \cdot (NH_3)_3$ but a transition state, ~3500 cm^{-1} above the enol.

The enol → HT1 step has a slightly higher barrier and is less exoergic than that of the ammonia wire. However, the overall enol → keto reaction is calculated to be 130 cm^{-1} more exoergic than for the $7HQ \cdot (NH_3)_3$ cluster. The calculated ESHAT reaction profile for the *3ch3*–AWW isomer of $7HQ \cdot NH_3 \cdot H_2O_2$ is shown in figure 24, together

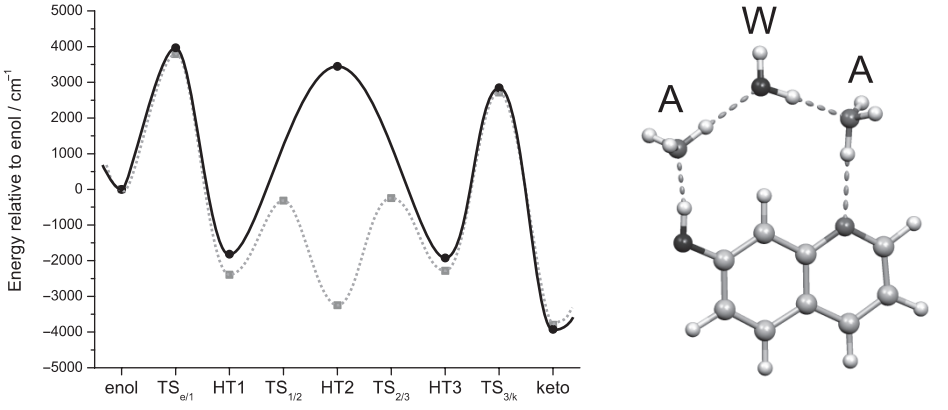

Figure 23. Left: CIS/6-31(+)G(d,p) ESHAT reaction profile for the *3ch3*–AWA isomer (full line), compared to that of $7HQ \cdot (NH_3)_3$ (dotted line). Both profiles are referenced to the energy of the enol cluster in the S_1 state. Right: minimum energy structure of the *3ch3*–AWA isomer.

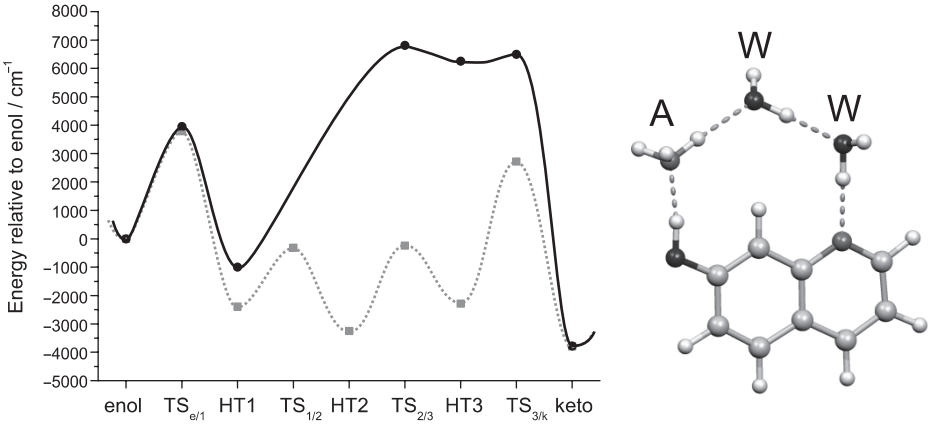

Figure 24. Left: CIS/6-31(+)G(d,p) ESHAT reaction profile for the *3ch3*–AWW isomer of $7HQ \cdot NH_3 \cdot H_2O_2$ (full line), compared to that of $7HQ \cdot (NH_3)_3$ (dotted line). Both profiles are referenced to the energy of the enol cluster in the S_1 state. Right: minimum energy structure of the *3ch3*–AWW isomer.

with that of $7HQ \cdot (NH_3)_3$ for reference. A total of two minima and three transition states were found along the ESHAT pathway. The enol → HT1 barrier $TS_{e/1}$ barrier is 3960 cm^{-1}, again slightly higher than for the ammonia-wire cluster. However, the HT1 minimum is raised significantly and the enol → HT1 exoergicity is reduced from −2390 cm^{-1} to −1000 cm^{-1}. No stationary points corresponding to $TS_{1/2}$ and HT2 could be found. The HT3 structure is predicted to be a shallow minimum, 6250 cm^{-1} above the enol form. The overall enol → keto exoergicity is again very similar to that of the ammonia-wire cluster.

5.3. *Discussion*

Figure 25 collects all four ESHAT potentials presented above. Relative to the $7HQ \cdot (NH_3)_3$ cluster, substitution of every NH_3 by an H_2O molecule raises the potential minima by 7000–8000 cm^{-1} and the transition states by 4000–7500 cm^{-1}.

For the water-wire cluster, even the first transition state $TS_{e/1}$ is raised significantly and the first reaction step is endoergic. Substitution of the central ammonia by H_2O in $7HQ \cdot (NH_3)_2 \cdot H_2O$ AWA leads to a perturbation of the ESHAT potential in the vicinity of HT2; exchange of the last two ammonia molecules leads to a potential that closely follows that of the pure water wire cluster in the last part, i.e. between $TS_{2/3}$ and keto. The relative energies of the HT1 forms also depend on the chain composition. The HT1 form of the ammonia wire AAA lies 2390 cm^{-1} below the

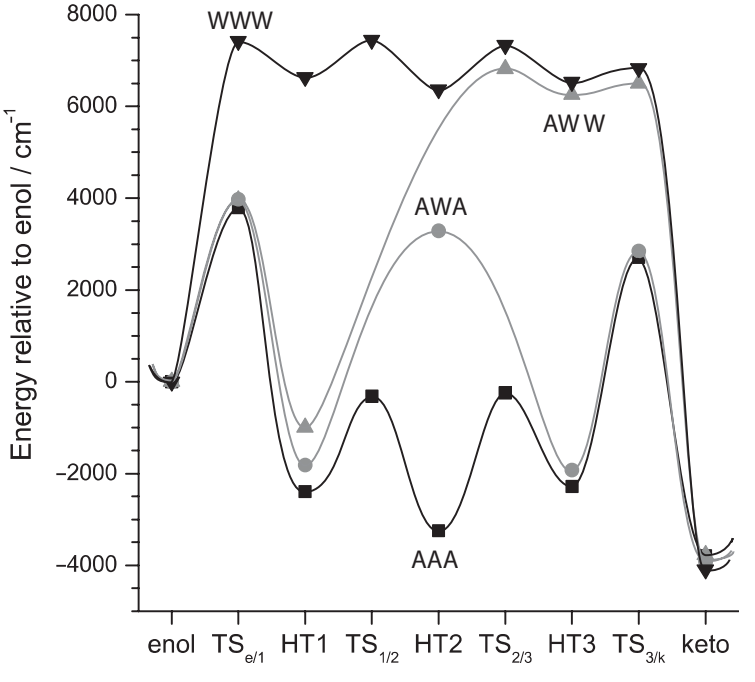

Figure 25. ESHAT potentials of the solvent-wire clusters: $7HQ \cdot (NH_3)_3$ (AAA), $7HQ \cdot (NH_3)_2 \cdot H_2O$ (AWA), $7HQ \cdot NH_3 \cdot (H_2O)_2$ (AWW) and $7HQ \cdot (H_2O)_3$ (WWW).

enol, for AWA only by 1820 cm^{-1} and for AWW by only 1000 cm^{-1}. The HT1 form of the $(H_2O)_3$ water wire WWW lies 6640 cm^{-1} *above* its enol form.

The R2PI spectra of the three mixed species AAW, AWA and AWW break off at increasing vibrational energies between 200 and 700 cm^{-1}, whereas there is no such indication for the pure water wire. Since the first step of the ESHAT reaction exhibits similar behaviour for the mixed wires and the pure ammonia wire but differs from the pure water wire (figure 25), we conclude that the breaking off of the R2PI signal is linked to the initial enol $\rightarrow$ HT1 step. All spectra that break off are solvent wires with an NH_3 molecule hydrogen-bonded to the O–H group of 7HQ, allowing the formation of a stabilized HT1 form.

For $7HQ \cdot (NH_3)_3$ we concluded from the large difference between the calculated energy barrier and the observed reaction threshold and from the H/D isotope effect that the $TS_{e/1}$ barrier is passed by tunnelling. Among the factors contributing to the tunnelling rate are: (1) the barrier height, (2) the effective (multidimensional) barrier width, and (3) the density of vibrational levels on the product side of the barrier at the energy of the tunnelling state [9]. From the relative energies of the HT1 forms and from the extent of H-atom delocalization shown in figure 25, we estimate that the density of product vibrational levels will be largest for the ammonia-wire AAA cluster, followed by the AWA and AWW clusters.

6. Conclusion

We have combined spectroscopic and quantum chemical methods to study the excited state hydrogen atom transfer (ESHAT) reactions along hydrogen-bonded solvent wires. 7-Hydroxyquinoline has proven to be an ideal scaffold and probe molecule for such studies:

(i) It provides a rigid structure to which hydrogen-bonded solvent wires of two, three or four solvent molecules such as H_2O or NH_3 can be attached in an unidirectional manner.
(ii) 7HQ is simultaneously a photoacid at its O–H group and a photobase at its ring nitrogen position. $S_1 \leftarrow S_0$ photoexcitation of 7HQ provides a means of generating a driving potential for H-atom transfer from the O–H towards the N heterocyclic position.
(iii) Passage of an H-atom along the wire converts the enol 7-hydroxyquinoline to its 7-ketoquinoline tautomer, inverting the hydrogen-bond directionality of the solvent wire.
(iv) The enol form exhibits UV fluorescence while the 7-ketoquinoline tautomer fluoresces in the yellow, providing a sensitive means of observing the eventual H-atom transfer.

We have analysed the low-lying electronic excited states of bare 7-hydroxyquinoline to understand the H-atom transfer reactions in the solvent-wire clusters. The lowest excited state of A″ symmetry ($\pi\sigma^*$) of 7-hydroxyquinoline is repulsive along the O–H stretching coordinate; note that this state is not optically accessible from the S_0 ground state. It crosses the optically accessible S_1 $\pi\pi^*$ state of A′ symmetry and at

large O–H distances even the S_0 state potential, becoming the electronic ground state. The O–H bond is broken homolytically, resulting in a hydrogen atom and a quinolinyl radical.

In supersonic molecular beams, NH_3 molecules can be successively added to 7HQ to form the ammonia-wire clusters $7HQ \cdot (NH_3)_n$. Their vibronic spectra are resolved by combinations of laser spectroscopic and mass spectrometric techniques. We find no experimental evidence for excited state reactivity up to a vibrational excess energy of $\approx 1000\,cm^{-1}$ for clusters with $n \leq 2$. The $7HQ \cdot (NH_3)_3$ cluster also shows sharp structured vibronic bands and UV fluorescence from the different vibronic bands as the smaller clusters. However, at excess vibrational energies above $\sim 200\,cm^{-1}$, both the R2PI and the UV fluorescence excitation spectra break off. Fluorescence action spectra of the yellow keto fluorescence prove that the 7-ketoquinoline $\cdot (NH_3)_3$ cluster is formed and that enol $\rightarrow$ keto tautomerization occurs, mediated by the ammonia solvent wire. The spectral breaking off represents the energy threshold at which the excited-state H-atom transfer (ESHAT) rate becomes competitive with the UV fluorescence rate.

Excited state *ab initio* calculations were used to model the reaction pathway. These reveal that the reaction has to be classified as H-atom (and not as a proton) transfer. The calculations also predict an excited state *proton* transfer pathway, but this lies at much higher energy than the ESHAT pathway in the ammonia-wire cluster.

In the ESHAT pathway, an electron moves along with the proton in a Grotthus type mechanism, forming intermediate NH_4 radicals that are distinct local minima along the reaction profile. The crossing of the optically excited $\pi\pi^*$ with a higher-lying $\pi\sigma^*$ state gives rise to a conical intersection, which determines the barrier height for the ESHAT reaction.

The initial enol $\rightarrow$ HT1 step of the ESHAT reaction was also analysed using an intrinsic reaction coordinate (IRC) approach. This allows one to decompose the first reaction step into three different phases, involving movement of heavy atoms or of the H-atom only. As the largest part of the barrier is passed in the light coordinate, tunnelling is expected to play an important role, in agreement with observation of the fully deuterated cluster: d_2-$7DQ \cdot (ND_3)_3$ shows an increased threshold for D-atom transfer compared to $7HQ \cdot (NH_3)_3$.

Additionally, we observe mode-selective tunnelling for both $7HQ \cdot (NH_3)_3$ and d_2-$7DQ \cdot (ND_3)_3$. The low-frequency *intra*molecular modes of 7HQ enhance the ESHAT reaction less efficiently than the *inter*molecular ammonia-wire stretching modes of similar frequency. The experimentally observed mode-selectivity was explained by the ability of a given mode to lower the energy difference between $\pi\pi^*$ and $\pi\sigma^*$ excited states.

Dramatic effects on ESHAT along the solvent wire occur when substituting NH_3 by H_2O molecules, as in the mixed ammonia-water clusters $7HQ \cdot (NH_3)_n \cdot (H_2O)_m$, $n + m = 3$. The introduction of a single H_2O blocks the complete ESHAT reaction, i.e. the enol $\rightarrow$ keto tautomerization pathway. The CIS calculations reveal that introduction of an H_2O molecules gives rise to a high barrier in the reaction profile. The initial enol $\rightarrow$ HT1 step is possible if the first position in the wire is occupied by one NH_3 molecule. These chemical substitution experiments show that the disappear-

ance of the R2PI signal is due to the onset of injection of the O–H hydrogen atom into the wire and not to the formation of the keto tautomer.

References

[1] M. Eigen, Angew. Chem. Int. Ed. **3,** 1 (1964).
[2] A. Weller, Progr. React. Kinet. **1,** 187 (1961).
[3] N. Agmon, Chem. Phys. Lett. **244,** 456 (1995).
[4] D. Borgis and J. T. Hynes, Chem. Phys. **170,** 315 (1993).
[5] D. Lu and G. A. Voth, J. Am. Chem. Soc. **120,** 4006 (1998).
[6] R. Vuilleumier and D. Borgis, J. Phys. Chem. B **102,** 4261 (1998).
[7] R. Vuilleumier and D. Borgis, J. Chem. Phys. **111,** 4251 (1999).
[8] H. S. Mei, M. E. Tuckerman, D. E. Sagnella and M. L. Klein, J. Phys. Chem. B **102,** 10446 (1998).
[9] R. I. Cukier and J. Zhu, J. Chem. Phys. **110,** 9587 (1999).
[10] P. K. Agarwal, S. P. Webb and S. Hammes-Schiffer, J. Am. Chem. Soc. **122,** 4803 (2000).
[11] J. T. Hynes, T.-H. Tran-Thi and G. Granucci, J. Photochem. Photobiol. A **154,** 3 (2002).
[12] Q. Cui and M. Karplus, J. Phys. Chem. B **106,** 7927 (2002).
[13] D. Marx, M. E. Tuckerman, J. Hutter and M. Parrinello, Nature **397,** 601 (1999).
[14] P. L. Geissler, C. Dellago, D. Chandler, J. Hutter and M. Parrinello, Science **291,** 2121 (2001).
[15] M. E. Tuckerman, D. Marx and M. Parrinello, Nature **417,** 925 (2002).
[16] M. H. B. Stowell, T. M. McPhillips, D. C. Rees, S. M. Soltis, E. Abresch and G. Feher, Science **276,** 812 (1997).
[17] Y. Y. Sham, I. Muegge and A. Warshel, Proteins: Structure, Function and Genetics **36,** 484 (1999).
[18] H. Luecke, B. Schobert, H.-T. Richter, J. P. Cartailler and J.K. Lanyi, J. Mol. Biol. **291,** 899 (1999).
[19] H. Luecke, B. Schobert, H.-T. Richter, J. P. Cartailler and J.K. Lanyi, Science **286,** 255 (1999).
[20] H. Luecke, Biochim. Biophys. Acta – Bioenergetics **1460,** 133 (2000).
[21] S. Subramaniam and R. Henderson, Nature **406,** 653 (2002).
[22] L. Baciou and H. Michel, Biochem. **34,** 7967 (1995).
[23] H. Michel, Proc. Natl. Acad. Sci. **95,** 12819 (1998).
[24] R. Pomès and B. Roux, Biophys. J. **82,** 2304 (2002).
[25] B. Roux, Acc. Chem. Res. **35,** 366 (2002).
[26] R. Pomès and C.-H. Yu, Front. Bioscience **8,** 1288 (2003).
[27] T. E. Decoursey, Physiol. Rev. **83,** 475 (2003).
[28] K. M. Jude, K. Wright, C. Tu, D. N. Silverman, R. E. Viola and D. W. Christianson, Biochem. **41,** 2485 (2002).
[29] Q. Cui and M. Karplus, J. Phys. Chem. B **107,** 1071 (2003).
[30] R. Pomès and B. Roux, Biophys. J. **71,** 19 (1996).
[31] R. Vuilleumier and D. Borgis, Chem. Phys. Lett. **284,** 71 (1998).
[32] H. Decornez and S. Hammes-Schiffer, Isr. J. Chem. **39,** 397 (1999).
[33] K. Murata, K. Mitsuoka, T. Hirai, T. Walz, P. Agre, J. B. Heymann, A. Engel and Y. Fujiyoshi, Nature **407,** 599 (2000).
[34] H. Sui, B.-G. Han, J. Lee, P. Walian and B. K. Jap, Nature **414,** 872 (2001).
[35] R. Dutzler, E. B. Campbell, M. Cadene, B. T. Chait and R. MacKinnon, Nature **415,** 287 (2002).
[36] B. L. de Groot, T. Frigato, V. Helms and H. Grubmüller, J. Mol. Biol. **333,** 279 (2003).
[37] E. Tajkhorshid, P. Nollert, M. Ø. Jensen, L. J. W. Miercke, J. O'Connell, R. M. Stroud and K. Schulten, Science **296,** 525 (2002).
[38] B. Ilan, E. Tajkhorshid, K. Schulten and G. A. Voth, Proteins – Structure, Function and Bioinformatics **55,** 223, (2004).
[39] A. Burykin and A. Warshel, Biophys. J. **85,** 3696 (2003).
[40] B. L. de Groot and H. Grubmüller, Curr. Opin. Struct. Biol. **15,** 176 (2005).
[41] M. Eigen, W. Kruse, G. Maass and L. De Maeyer, Progr. React. Kinet. **2,** 285 (1964).
[42] S. F. Mason, J. Philip and B. E. Smith, J. Chem. Soc. A, 3051 (1968).
[43] S. Schulman and Q. Fernando, Tetrahedron **24,** 1777 (1968).
[44] E. Bardez, Isr. J. Chem. **39,** 319 (1999).
[45] A. Lavin and S. Collins, J. Phys. Chem. **97,** 13615 (1993).
[46] A. Bohra, A. Lavin and S. Collins, J. Phys. Chem. **98,** 11424 (1994).
[47] P. J. Thistlethwhaite and P. J. Corkill, Chem. Phys. Lett. **85,** 317 (1982).
[48] P. J. Thistlethwhaite, Chem. Phys. Lett. **96,** 509 (1983).

[49] M. Itoh, T. Adachi and K. Tokumura, J. Am. Chem. Soc. **106,** 850 (1984).
[50] T.-G. Kim, S.-I. Lee, D.-J. Jang and Y. Kim, J. Phys. Chem. **99,** 12698 (1995).
[51] S.I. Lee and D.J. Jang, J. Phys. Chem. **99,** 7537 (1995).
[52] T. Nakagawa, S. Kohtani and M. Itoh, J. Am. Chem. Soc. **117,** 7952 (1995).
[53] I. García-Ochoa, P.B. Bisht, F. Sánchez, E. Martinez-Atáz, L. Santos, H. B. Tripathi and A. Douhal, J. Phys. Chem. A **102,** 8871 (1998).
[54] P.-T. Chou and C.-Y. Wei, J. Phys. Chem. B **102,** 3305 (1998).
[55] P.-T. Chou, C.-Y. Wei, C.-R. C. Wang, F.-T. Hung and C. P. Chang, J. Phys. Chem. A **103,** 1939 (1999).
[56] S. Kohtani, A. Tagami and R. Nakagaki, Chem. Phys. Lett. **316,** 88 (2000).
[57] X. Dong, Z. Guilan, W. Haiyan, T. Guoqing and C. Wenju, Chem. Phys. Lett. **318,** 433 (2000).
[58] H. Yu, O. H. Kwon and D.-J. Jang, J. Phys. Chem. A **108,** 5932 (2004).
[59] A. L. Sobolewski and W. Domcke, J. Phys. Chem. A **103,** 4494 (1999).
[60] A. L. Sobolewski and W. Domcke, Phys. Chem. Chem. Phys. **1,** 3065 (1999).
[61] A. L. Sobolewski and W. Domcke, Chem. Phys. Lett. **315,** 293 (1999).
[62] A. L. Sobolewski and W. Domcke, Chem. Phys. **259,** 181 (2000).
[63] A. L. Sobolewski and W. Domcke, J. Phys. Chem. A **105,** 9275 (2001).
[64] A. L. Sobolewski, W. Domcke, C. Dedonder-Lardeux and C. Jouvet, Phys. Chem. Chem. Phys. **4,** 1093 (2002).
[65] A. L. Sobolewski and W. Domcke, Eur. Phys. J. D **20,** 369 (2002).
[66] A. L. Sobolewski and W. Domcke, Chem. Phys. Lett. **300,** 533 (1999).
[67] A. L. Sobolewski and W. Domcke, Chem. Phys. Lett. **329,** 130 (2000).
[68] A. L. Sobolewski and W. Domcke, Phys. Chem. Chem. Phys. **6,** 2763 (2004).
[69] V. Vallet, Z. G. Lan, S. A. Mahapatra, A. L. Sobolewski and W. Domcke, Faraday Discuss. **127,** 283 (2004).
[70] F. Lahmani, A. Douhal, E. Breheret and A. Zehnacker-Rentien, Chem. Phys. Lett. **220,** 235 (1994).
[71] A. Bach and S. Leutwyler, Chem. Phys. Lett. **299,** 381 (1999).
[72] A. Bach, S. Coussan, A. Müller and S. Leutwyler, J. Chem. Phys. **112,** 1192 (2000).
[73] A. Bach and S. Leutwyler, J. Chem. Phys. **112,** 560 (2000).
[74] S. Coussan, A. Bach and S. Leutwyler, J. Phys. Chem. A **104,** 9864 (2000).
[75] S. Coussan, M. Meuwly and S. Leutwyler, J. Chem. Phys. **114,** 3524 (2001).
[76] M. Meuwly, A. Bach and S. Leutwyler, J. Am. Chem. Soc. **123,** 11446 (2001).
[77] A. Bach, C. Tanner, C. Manca, H.-M. Frey and S. Leutwyler, J. Chem. Phys. **119,** 5933 (2003).
[78] S. Coussan, C. Manca, C. Tanner, A. Bach and S. Leutwyler, J. Chem. Phys. **119,** 3774 (2003).
[79] A. Bach, S. Coussan, A. Müller and S. Leutwyler, J. Chem. Phys. **113,** 9032 (2000).
[80] C. Manca, C. Tanner, S. Coussan, A. Bach and S. Leutwyler, J. Chem. Phys. **121,** 2578 (2004).
[81] C. Tanner, C. Manca and S. Leutwyler, Science **302,** 1736 (2003).
[82] C. Tanner, C. Manca and S. Leutwyler, J. Chem. Phys. **122,** 204326 (2005).
[83] C. Tanner, C. Manca and S. Leutwyler, Chimia **58,** 234 (2004).
[84] O. David, C. Dedonder-Lardeux and C. Jouvet, Int. Rev. Phys. Chem. **21,** 499 (2002).
[85] K. Daigoku, S. Ishiuchi, M. Sakai, M. Fujii and K. Hashimoto, J. Chem. Phys. **119,** 5149 (2003).
[86] S. Ishiuchi, K. Daigoku, K. Hashimoto and M. Fujii, J. Chem. Phys. **120,** 3215 (2004).
[87] C. Manca, C. Tanner and S. Leutwyler, Chimia **58,** 287 (2004).
[88] R. I. Cukier, J. Phys. Chem. B **106,** 1746 (2002).
[89] A. Suárez and R. Silbey, J. Chem. Phys. **94,** 4809 (1991).
[90] D. Borgis and J. T. Hynes, J. Chem. Phys. **94,** 3619 (1991).
[91] A. Soudackov and S. Hammes-Schiffer, J. Chem. Phys. **113,** 2385 (2000).
[92] S. Y. Kim and S. Hammes-Schiffer, J. Chem. Phys. **119,** 4389 (2003).
[93] C. Tanner, M. Thut, A. Steinlin, C. Manca and S. Leutwyler, J. Phys. Chem. in press (2005).